The Pennsylvania State University

The Graduate School

Eberly College of Science

PHASE-DETERMINING FACTORS IN THE COLLOIDAL SYNTHESIS OF METASTABLE TRANSITION-METAL CHALCOGENIDE NANOCRYSTALS

A Thesis in

Chemistry

by

Anna E. Powell

Submitted in Partial Fulfillment
of the Requirements
for the Degree of

Master of Science

May 2016

The thesis of Anna E. Powell was reviewed and approved* by the following:

Raymond E. Schaak
DuPont Professor of Materials Chemistry
Thesis Adviser

Miriam A. Freedman
Assistant Professor of Chemistry

Benjamin J. Lear
Assistant Professor of Chemistry

Kenneth S. Feldman
Professor of Chemistry
Chemistry Graduate Program Chair

*Signatures are on file in the Graduate School.

Abstract

In nanochemistry, it is a common goal to be able to synthesize materials with a specific morphology, composition, size, and crystal structure. This type of synthetic control is desirable as even small changes in one of these four factors can lead to drastically different material properties. An example of this is the formation of non-equilibrium crystal phases which are metastable in bulk systems and often exhibit characteristics unique from the thermodynamically stable phase. Consequently, these metastable phases are favored for certain applications due to their properties. However, attempts to synthesize a phase pure sample of a non-equilibrium crystal phase are often fraught with difficulties as phase determining factors are not well understood for nanoscale syntheses. As a result, nanoscale synthetic research is frequently performed in an exploratory, semi-serendipitous method. It is therefore desirable to expand our understanding of nanoscale reactions so as to facilitate the directed synthesis of specific nanoscale targets.

In the research reported herein, attempts were made to elucidate the phase determining factors in two systems: polyol synthesis of manganese(II) sulfide, and cation exchange with cobalt and manganese. First, a manganese(II) sulfide, MnS, polyol synthesis was studied to elucidate which reaction variables have the greatest impact in crystal phase determination. Initial research showed that reaction temperature, aging time, and manganese source had the greatest influence on the crystal phase of the MnS product. Further investigation of this reaction implied that a complex relationship exists between the decomposition rate of the sulfur source, the concentration of the tetramethylammonium hydroxide pentahydrate, and the presence of an *in situ* intermediate. Although this complex relationship was not deconvoluted through this

research, these results nevertheless help to shed light on the phase determining factors in the polyol synthesis of manganese(II) sulfide.

In addition, cation exchange was investigated as a method for the synthesis of metastable phases. Although the use of ion exchange to access metastable phases had been reported previously, much of this research was limited to copper, silver, cadmium, lead and zinc chalcogenides. In this work, cation exchange with cobalt and manganese from a roxbyite-type $Cu_{2-x}S$ precursor was explored. Ultimately, metastable wurtzite-type cobalt- and manganese sulfides were synthesized through this exchange process. This result is of great interest for several reasons. First of all, cation exchange was performed with two transition metal cations which had previously only served as dopants in exchange reactions. This work also demonstrates a colloidal method for the synthesis of wurtzite-type CoS which had previously only been synthesized through chemical bath deposition methods. Finally, formation of the metastable wurtzite-type phases demonstrates the retention of both anion and cation sublattice features – a result which has not been reported in literature to date.

Table of Contents

List of Figures

List of Tables

List of Abbreviations

α-MnS (rocksalt-type manganese sulfide)

β-MnS (zinc blende-type manganese sulfide)

γ-MnS (wurtzite-type manganese sulfide)

ccp (cubic-close packed)

CVD (chemical vapor deposition)

DMS (dilute magnetic semiconductor)

EDS (energy-dispersive X-ray spectroscopy)

fcc (face-centered cubic)

HAADF-STEM (high angle annular dark field scanning transmission electron microscopy)

hcp (hexagonal-close packed)

HRTEM (high-resolution transmission electron microscopy)

HSAB (hard-soft acid-base)

LDH (layered double hydroxide)

MBE (molecular beam epitaxy)

RPM (revolutions per minute)

SAED (selected area electron diffraction)

STEM-EDS (scanning transmission electron microscopy energy-dispersive X-ray spectroscopy)

TEM (transmission electron microscopy)

TMAOH (tetramethylammonium hydroxide pentahydrate)

TMC (transition metal chalcogenide)

TOP (tri-*n*-octylphosphine)

XRD (X-ray diffraction)

Acknowledgements

First of all, I would like to thank my research adviser, Dr. Raymond Schaak, for his guidance during my graduate career and his support as I began exploring different career options. I would also like to thank my committee members, Dr. Benjamin Lear and Dr. Miriam Freedman for their help and advice.

I would also like to thank the Schaak Group members who I have had the pleasure of working with the past two-and-a-half years. In particular, I would like to thank Dr. Eric Popczun and Carlos Read for taking me under their wings as a first-year. I always appreciated their willingness to answer questions and provide assistance when I needed help.

Next, I have to thank all of the amazing teachers who sparked my love of teaching and helped me to get where I am today—Mrs. Jeanne Rust, Mr. Ted Hallberg, Mrs. Anna Chenoweth, Dr. George Bandik, and Dr. Jill Millstone. I only hope that I may touch the lives of my students like you have touched mine. I would also like to thank Dr. Jackie Bortiatynski for all of her patience, advice, and support as I explored the field of chemical education and future career opportunities.

Finally, I have to thank my family—my parents, Jim and Barbara Powell, and my brother Brian. Words simply cannot express how much your constant love and support have meant to me. Through good times and bad, you have always been there offering advice, encouragement, and a kind ear to listen. I never would have been able to do this without you—from the deepest depths of my heart, thank you.

CHAPTER 1. INTRODUCTION

Introduction to Nanomaterials

Within the past six decades,[1] the field of nanomaterials has expanded to include a vast array of materials such as graphene,[2] quantum dots,[3] and metallic nanocrystals.[4] These materials, as well as many other nanomaterials, have garnered great interest due to potential applications in medicine,[5] technology,[6] and alternative energy[7] resources arising from their unique properties. Nanomaterials, defined as having at least one dimension between 1 and 100 nm, are unique in that they bridge the atomic and macroscopic realms. As a result, nanomaterials often exhibit interesting and useful optical, electronic, and physical properties.[8] In all of these cases, the properties of the material are dependent upon the composition, morphology, crystal structure, and size. By fine-tuning these components, it becomes possible to alter the properties of the resultant material.

Nanoscale Synthetic Techniques

There are two main categories of techniques used in the synthesis of nanomaterials: top-down and bottom-up approaches. In top-down methods, such as photolithography,[9] ball milling,[10] and laser ablation,[11] bulk material is carved away to yield materials with nanoscale dimensions. Although top-down approaches are frequently used in manufacturing due to their excellent reproducibility, these techniques also have limitations. As the products of top-down techniques are formed out of bulk materials, crystal structures that are present only at the nanoscale regime are inaccessible. In addition, many nanolithographic methods are limited in their resolution. As a result, bottom-up synthetic methods are often desirable as a greater variety of materials can be accessed.

There are a vast number of bottom-up synthetic methods including chemical vapor deposition (CVD),[12] molecular beam epitaxy (MBE),[13] and colloidal synthesis.[14] Colloidal synthesis, which will be the focus of the research discussed herein, is of particular interest for large-scale manufacturing due to its scalability and ease of processability. Generally in colloidal nanoparticle synthesis, metal precursor salts are combined with a capping agent and a reducing agent in either a polar or non-polar solvent. During synthesis, the capping agent serves as a surfactant helping to coat the nanoparticles. This prevents aggregation and aids in the suspension of the nanoparticles to form a semi-homogenous solution. It is important to note that the solvent can adopt several roles in colloidal synthesis. Beyond serving as a reaction medium, the solvent can also serve as a capping agent and/or reducing agent. For example, in polyol reactions, a metal salt is combined with a high boiling point alcohol (commonly ethylene glycol or polyethylene glycol) and heated to cause nucleation of the metal particles. Using this method, a variety of materials can be produced including copper, cobalt, nickel, cadmium, and lead particles.[15] Building upon the colloidal synthesis scaffold, it becomes possible to access a greater array of materials by adding additional reactive species such as chalcogenide or phosphide precursors, including multiple metal precursors, or changing the reducing agent, capping agent, or solvent. In addition, changes to reaction attributes, such as the amount of headspace in a reaction vessel, the heating ramp rate, and the rate of stirring, can be used to further tune the product characteristics.

Although great complexity exists within the realm of colloidal nanoparticle synthesis, many reactions share a similar reaction set-up, shown in *Figure 1*. In the basic apparatus, a 3-neck round bottom flask containing a stir bar is placed over a stir plate. If needed, a heating mantle can be used to heat the solution during the synthesis. A glass condenser is then connected

to the flask and can be attached to either a Schlenk line or bubbler depending upon the requirements of the reaction. Temperature can also be monitored through the use of thermometer or a thermocouple. Although a glass stopper can be used to seal the third neck of the flask, a rubber septa allows for subsequent injections through use of a syringe.

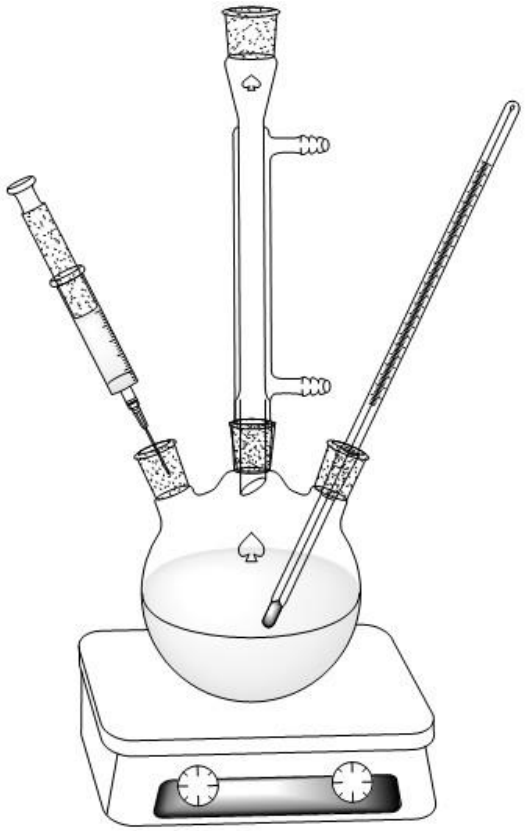

Figure 1: Example colloidal synthesis apparatus. A 3-neck round bottom flask is connected to a condenser and either a thermometer or thermocouple probe. The third neck of the flask is then sealed with a rubber septa which allows for injections using a syringe. Illustration drawn by Anna E. Powell.

Phase Determining Factors

In contrast to traditional solid-state synthesis techniques, colloidal synthesis employs much lower reactions temperatures. These lower reaction temperatures, combined with the unique characteristics of nanoscale systems, permits the formation of crystal phases which are

not observed at the bulk scale. These crystal phases, commonly referred to as *metastable phases* are stabilized at certain size, temperature, and pressure regimes; however, these metastable phases will transform into the thermodynamic phase upon heating. It is vital that we are able to access these metastable phases as they often exhibit unique properties compared to the thermodynamic phase. For example, the thermodynamic 2H phase of MoS_2 is a semiconducting material, whereas the metastable 1T MoS_2 phase is metallic. This fact is due to differences in the spatial arrangements of the atoms where the 1T phase has a distorted octahedral coordination and the 2H phase has trigonal prismatic coordination. As a result, the density of states of the 1T phase is much higher which allows for improved flow of electrons and a 10^7 increase in conductivity over the 2H phase.[16-17]

In literature, many factors are attributed to the formation of metastable phases at the nanoscale. However, three factors are routinely cited. The first factor is kinetic contributions which can be broadly described using the LaMer diagram, *Figure 2*. At the start of a reaction, the main process occurring is the dissolution of the metal precursor into monomer species, regime I. Once the monomer concentration reaches a minimum threshold, C^*_{min}, nucleation occurs until such time that the monomer concentration drops below this threshold, signaling the end of regime II. In regime III, monomer diffusion allows the continued growth of nuclei formed during regime II.[18] Although the LaMer diagram provides a model for understanding particle nucleation and growth, it is important to remember that a variety of factors can alter the kinetics of nanoparticle synthesis including ligand strength, the ability of the solvent to coordinate with reactive species, and the decomposition rate of precursor materials.

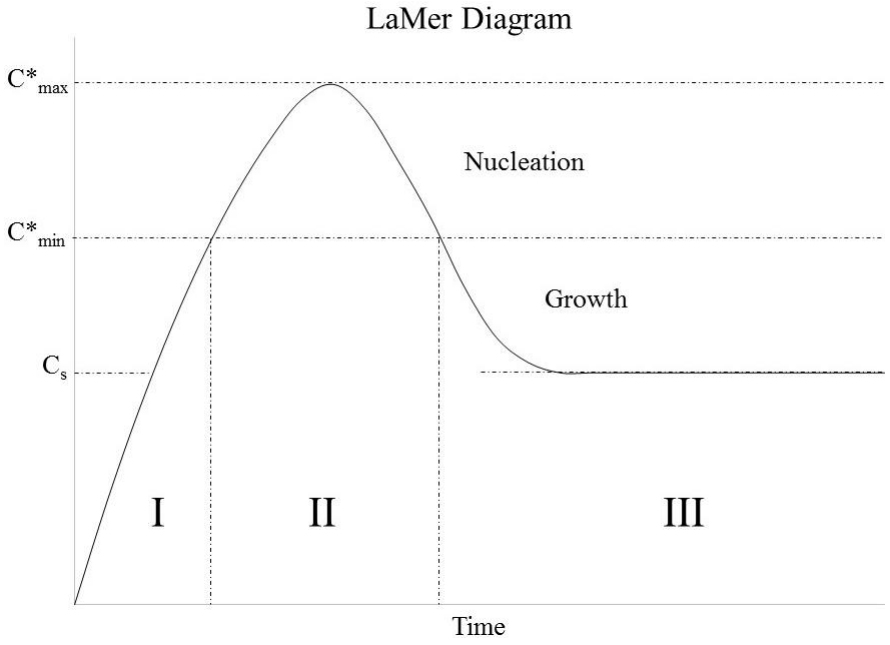

Figure 2: LaMer Diagram depicting the kinetics of nanoparticle nucleation and growth. Regime I – formation of monomers, Regime II – nucleation of particles, Regime III – particle growth. Illustration drawn by Anna E. Powell.

Another key consideration in the formation of metastable phases is the thermodynamics of the system. As nanoparticles have a significantly larger surface area compared to their bulk counterparts, the interactions of surface atoms with their surroundings play a much larger role in the energetics of nanoscale systems. In general, atoms with more dangling bonds will be more reactive. This is shown by the fact that atoms at edges or corners of a material tend to have higher reaction rates than particles on the face of a material, *Figure 3a*.[19] Additionally, as smaller particles have a higher radius of curvature, they also have a more reactive surface. As is shown in *Figure 3b*, the smallest particle has the shortest radius and therefore the highest radius of curvature. In order to minimize this high energy state, Ostwald ripening will occur whereby smaller, more reactive particles will dissolve releasing monomers into solution. These monomers will then diffuse through the solution and bind with larger particles to decrease the

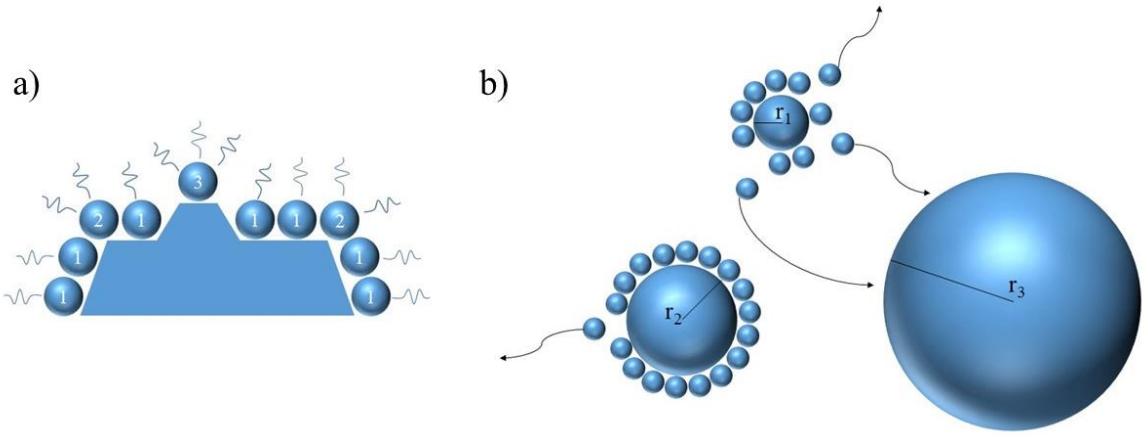

Figure 3: (a) depiction of dangling bonds on the surface atoms of a material, and (b) depiction of Ostwald ripening where $r_1 < r_2 < r_3$. Illustration drawn by Anna E. Powell.

overall energy of the system.[20] Although Ostwald ripening is energetically favorable, this process can be detrimental in nanoparticle synthesis as it can be difficult to produce very small particles (<10 nm). In order to counter the reactivity of nanoparticle surfaces, ligands serving as capping agents can help to minimize the energetics of the system and prevent processes such as Ostwald ripening from occurring.

Finally, *in situ* intermediates can help to determine the crystal phase of a product by serving as a template. Although *in situ* intermediates can form in a variety of reactions, a tangible example of *in situ* intermediate templating crystal growth is in the process of ion exchange, *Figure 4*.[21] In ion exchange, cations or anions from solution selectively replace their corresponding ionic counterpart in the crystal lattice. Through this process, partial or full ion exchange is possible.[22] In addition, subsequent exchanges can be used to induce a complete compositional transformation from the starting material.[23] As either the cation or anion sublattice is replaced in a reaction, the remaining unaltered sublattice can serve as a template to direct the placement of the exchanging ions. Although certain factors will sometimes play a

predominant role in crystal phase determination for a particular reaction, these factors generally work in concert to subtly influence the final nanocrystal product.

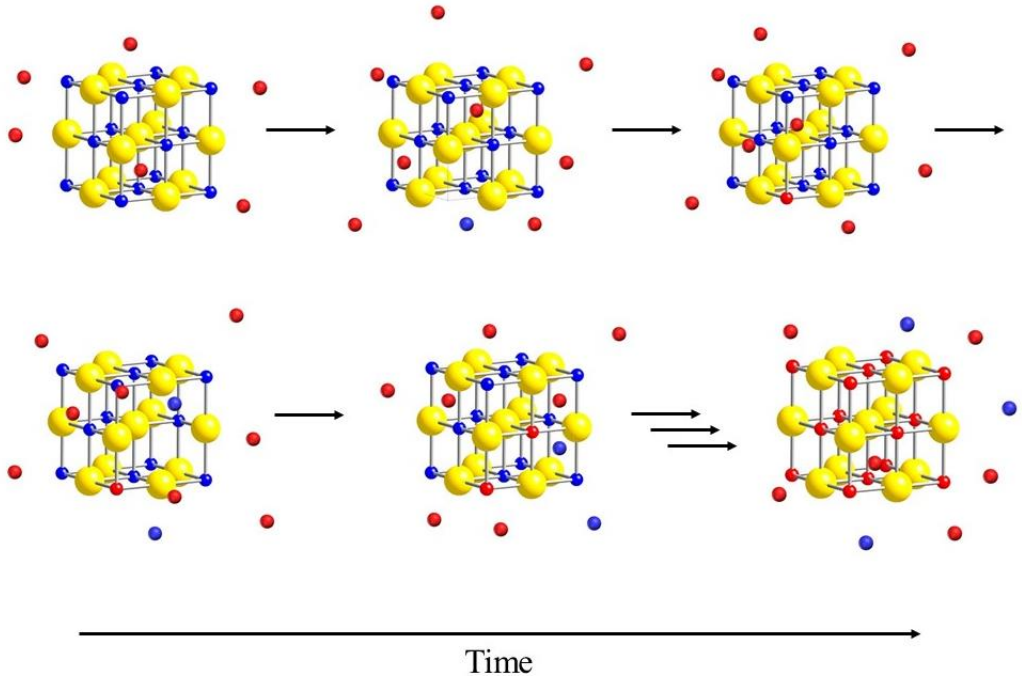

Figure 4: Depiction of cation exchange. Over the course of the exchange, the red cations intercalate into the crystal structure and replace the blue cations which were part of the original crystal lattice. In the end, the crystal lattice is composed entirely of the red cations and yellow anions with the blue cations existing in solution.

General Experimental Goals and Strategies

The following chapters build upon the common theme of accessing metastable crystal phases of transition metal chalcogenides through colloidal synthesis techniques. In chapter two, published literature preparations for manganese sulfide were studied in an attempt to elucidate methods for selectively synthesizing phase-pure α-, β-, and γ-MnS. This type of detailed study is necessary as there is very little understanding about which factors ultimately lead towards formation of a particular crystal phase. In this work, the recurring presence of a crystalline material, most consistent with a manganese layered double hydroxide, was hypothesized to act as

an *in situ* template for the formation of α-MnS due to similarities in the manganese coordination between the two structures. Although this hypothesis was ultimately disproven, this research helped to provide further insight into the role of certain factors in the formation of manganese sulfide.

In chapter three, cation exchange was explored for use in the synthesis of metastable transition metal chalcogenides. Through this work, it was found that roxbyite-type copper sulfide, $Cu_{2-x}S$, could undergo exchange with Co^{2+} and Mn^{2+} cations to form wurtzite-type CoS and MnS, respectively. These results are of great interest for several reasons. First of all, this work extends the realm of full-cation exchange to two transition metals which were previously understudied. Secondly, it is critical to note the formation of wurtzite-type CoS through this process. Previous to this work, wurtzite-type CoS had only been reported as a thin-film formed via chemical vapor deposition. Additionally, it is important to note that wurtzite-type CoS forms in opposition to the thermodynamic NiAs-type crystal structure. Due to this result, it is hypothesized that both anion and cation sublattice features can be retained through cation exchange to template the crystal phase of the product.

References

1. Feynman, F. P. There's Plenty of Room at the Bottom: An Invitation to Enter a New Field of Physics. *Reson.* **2011**, *16*, 890-905.

2. Geim, A.K.; Novoselov, K. S. The Rise of Graphene. *Nat. Mater.* **2007**, *6*, 183-191.

3. Alivisatos, A. P. Semiconductor Clusters, Nanocrystals, and Quantum Dots. *Science* **1996**, *271*, 933-936.

4. Turkevich, J.; Stevenson, P. C.; Hillier, J. A Study of the Nucleation and Growth Processes in the Synthesis of Colloidal Gold. *Discuss. Faraday Soc.* **1951**, *11*, 55-75.

5. Peer, D.; Karp, J. M.; Hong, S.; Farokhzad, O. C.; Margalit, R.; Langer, R. Nanocarriers as an emerging platform for cancer therapy. *Nat. Nanotechnol.* **2007**, *2*, 751-760.

6. Franklin, A. D. Nanomaterials in transistors: From high-performance to thin-film applications. *Science*. **2015**, *349*, aab2750.

7. Lewis, N. S. Towards Cost-Effective Solar Energy Use. *Science*. **2007**, *315*, 798-801.

8. Alivisatos, A. P. Perspectives on the Physical Chemistry of Semiconductor Nanocrystals. *J. Phys. Chem.* **1996**, *100*, 13226-13239.

9. Fourkas, J. T. Nanoscale Photolithography with Visible Light. *J. Phys. Chem. Lett.* **2010**, *1*, 1221-1227.

10. Baláž, P.; Achimovičova, M.; Baláž, M.; Billik, P.; Cherkezova-Zheleva, Z.; Criado, J. M.; Delogu, F.; Dutková, E.; Gotor, F. J.; Gaffet, E.; Kumar, R.; Mitov, I.; Rojac, T.; Senna, M.; Streletskii, A.; Wieczorek-Ciurowam, K. Hallmarks of mechanochemistry: from nanoparticles to technology. *Chem. Soc. Rev*. **2013**, *42*, 7571-7637.

11. Zeng, H.; Du, X.-W.; Sing, S. C.; Kulinich, S. A.; Yang, S.; He, J.; Cai, W. Nanomaterials via Laser Ablation/Irradiation in Liquid: A Review. *Adv. Funct. Mater.* **2012**, *22*, 1333-1353.

12. Shi, Y.; Li, H.; Li, L. Recent advances in controlled synthesis of two-dimensional transition metal dichalcogenides *via* vapour deposition techniques. *Chem. Soc. Rev.* **2015**, *44*, 2744-2756.

13. Panish, M. B. Molecular Beam Epitaxy. *Science*. **1980**, *208*, 916-922.

14. Kim, J. Y.; Voznyy, O.; Zhitomirsky, D.; Sargent, E. H. 25th Anniversary Article: Colloidal Quantum Dot Materials and Devices: A Quarter-Century of Advances. *Adv. Mat.* **2013**, *25*, 4986-5010.

15. Fievet, F.; Lagier, J. P.; Blin, B.; Beaudoin, B.; Figlarz, M. Homogenous and Heterogeneous Nucleations in the Polyol Process for the Preparation of Micron and Submicron Size Metal Particles. *Solid State Ionics*. **1989**, *32/33*, 198-205.

16. Huang, X.; Zeng, Z.; Zhang, H. Metal dichalcogenide nanosheets: preparation, properties, and applications. *Chem. Soc. Rev.* **2013**, *42*, 1934-1946.

17. Acerce, M.; Voiry, D.; Chhowalla, M. Metallic 1T phase MoS_2 nanosheets as supercapacitor electrode materials. *Nat. Nanotechnol.* **2015**, *10*, 313-318.

18. LaMer, V. K.; Dinegar, R. H. Theory, Production and Mechanism of Formation of Monodispersed Hydrosols. *J. Am. Chem. Soc.* **1950**, *72*, 4847-4854.

19. Lemke, B. P.; Haneman, D. Dangling bonds on silicon. *Phys. Rev. B.* **1978**, *17*, 1893-1907.

20. Yao, J. H.; Elder, K. R.; Guo, H.; Grant, M. Theory and simulation of Ostwald Ripening. *Phys. Rev. B.* **1993**, *47*, 14110-14125.

21. Liu, Y.; Goebl, J.; Yin, Y. Templated synthesis of nanostructured materials. *Chem. Soc. Rev.* **2013**, *42*, 2610-2653.

22. Son, D. H.; Hughes, S. M.; Yin, Y.; Alivisatos, A.P. Cation Exchange Reactions in Ionic Nanocrystals. *Science*. **2004**, *306*, 1009-1012.

23. J.M. Hodges, K. K., J.L. Fenton, C.G. Read, R.E. Schaak, Sequential Anion and Cation Exchange Reactions for Complete Material Transformations of Nanoparticles with Morphological Retention. *Angew. Chem. Int. Ed.* **2015,** *54*, 8669-8672.

CHAPTER 2. METASTABLE MANGANESE SULFIDE PHASES

Crystal Phases of Manganese Sulfide

Manganese sulfide, MnS, is a transition metal chalcogenide (TMC) that is of great interest due to potential applications in photochemical reactions,[1] short wavelength optoelectronic devices,[2] and lithium-ion batteries.[3] With a band gap of 3.7 eV, manganese sulfide is a semiconductor. In addition, some MnS crystal structures exhibit magnetic properties arising from superexchange.[4] These traits are two key properties of dilute magnetic semiconductor systems (DMS) such as $Zn_{1-x}Mn_xS$ and $Cd_{1-x}Mn_xS$ and make manganese sulfide an important end member in these systems.[5] Due to the many potential applications of MnS, it is therefore vital that its properties, structures, and syntheses are well characterized.

Manganese sulfide is interesting as three different crystal structures are routinely accessible at the nanoscale: α-MnS, rocksalt; β-MnS, zinc blende; and γ-MnS, wurtzite, *Figure*

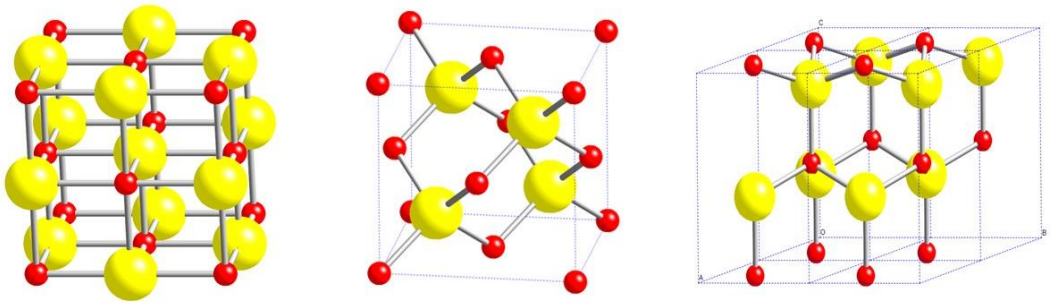

Figure 5: The three most common crystal phases of manganese sulfide (L to R): α-MnS, rocksalt; β-MnS, zinc blende; and γ-MnS, wurtzite. The manganese cations are red and the sulfur anions are yellow.

5. It should be noted that a recent report proved the existence of MnP-type manganese sulfide. This fourth phase is formed through high pressure distortions of the rocksalt crystal structure which causes polyhedral tilting.[6] As this MnP-type MnS has only be accessed through high pressure synthesis with a diamond anvil cell, it will not be discussed further.

The thermodynamic phase, α-MnS, consists of manganese and sulfur atoms in octahedral coordination with an ABC close packed ion stacking sequence, also known as a cubic close packed (ccp) lattice. The other two phases, β-MnS and γ-MnS, are metastable phases for manganese sulfide. As discussed in chapter 1, due to the unique properties of nanoscale systems, metastable phases can be stabilized at the nanoscale. In contrast to the thermodynamic phase, the ions in β- and γ-MnS are tetrahedrally coordinated. In the case of β-MnS, the ions still adopt face-centered cubic (fcc) lattice positions as in α-MnS. For γ-MnS, the ions adopt a hexagonal close packed (hcp) lattice, which is characterized by AB ion stacking.[4]

Due to the different crystal structures that manganese sulfide can adopt, it can exhibit a wide variety of properties. At the nanoscale, α-MnS is a green crystal whereas β- and γ-MnS adopt a pink hue.[7] Manganese sulfide also exhibits a shift in its photoluminescence spectra as octahedrally-coordinated MnS has an emission band at 1.45 eV whereas tetrahedrally-coordinated MnS has two emission bands at 1.75 and 1.95 eV.[8] The metastable crystal phases also exhibit distinct magnetic properties as both β- and γ-MnS are antiferromagnetic with Néel temperatures of 152 K and 90 K, respectively.[9] Although these are only some of the differences between the three crystal structures, they help to illustrate the many ways that structure can influence the properties of a material. In order to access these properties, it is important that we are able to selectively synthesize a particular manganese sulfide crystal phase.

To date, manganese sulfide has been synthesized using a variety of methods including colloidal,[10] solvothermal,[11] microwave irradiation,[12] molecular beam epitaxy,[13] and chemical vapor deposition methods.[14] However, literature preparations generally do not discuss the underlying factors which contribute to synthesis of a particular phase. The goal of this work was to perform a detailed study of published literature preparations for manganese sulfide to identify and study the underlying factors which have the greatest impact on the crystal phase of the product.

Experimental

Materials

Manganese(II) chloride tetrahydrate [99% trace metal basis], manganese(II) acetate tetrahydrate, sulfur powder [-325 mesh, 99.5%], and thiourea [99%] were purchased from Alfa Aesar. Oleylamine [technical grade, 70%], 1-octadecene [technical grade, 90%], oleic acid [technical grade, 90%], and tetramethylammonium hydroxide pentahydrate [≥97%] were purchased from Sigma Aldrich. Ethylene glycol [99.0+ %], as well as hexanes, ethanol, and acetone, all analytical grade, were purchased from VWR. All chemicals were used as received.

Methods

Standard Polyol Synthesis of Manganese Sulfide Particles: Adapting a previously published ZnS polyol procedure,[15] 217 mg manganese(II) chloride tetrahydrate (1.1 mmol), 790 mg tetramethylammonium hydroxide pentahydrate (4.4 mmol), and 7.5 mL ethylene glycol were heated at 120 °C for 10 min in a 50 mL 3-neck round bottom flask connected to a bubbler. A solution of 84 mg thiourea (1.1 mmol) dissolved via sonication in 7.5 mL ethylene glycol, was

then added. The reaction was then heated at 155 °C for 2 hours before cooling to room temperature. The particles were then cleaned with ethanol and hexanes via centrifugation before storing in ethanol. This standard synthesis was then altered to systematically study the impact of single variables. Variables studied include the reaction temperature, particle aging time, solvent choice, sulfur source, manganese source, the amount of tetramethylammonium hydroxide pentahydrate used, and the relative manganese and sulfur ratios.

Polyol Control Reaction: In a 50 mL 3-neck round bottom flask connected to a bubbler, 217 mg manganese(II) chloride tetrahydrate (1.1 mmol), 790 mg tetramethylammonium hydroxide pentahydrate(4.4 mmol), and 15 mL ethylene glycol were heated at 120 °C for 10 min. The reaction was then heated at 155 °C for 2 hours before cooling to room temperature. The reaction mixture was centrifuged at 12,000 RPM for 5 min and the supernatant was decanted into a labeled vial. The pellet was then cleaned three times with acetone via centrifugation at 12,000 RPM for 3 min before suspending in 7.5 mL ethylene glycol.

Synthesis of Wurtzite-Type MnS from the Control Reaction Supernatant: The supernatant from the polyol control reaction was combined with 67 mg thiourea (0.89 mmol) in a 50 mL 3-neck round bottom flask with a bubbler. The reaction was heated at 120 °C for 10 min before heating at 168 °C for 4 hours. Upon heating at 168 °C, the reaction mixture was a transparent blue hue which slowly became an opaque tan color. The reaction mixture was then cooled to room temperature and the particles were cleaned via centrifugation with acetone. The pellet was then stored in ethanol.

Synthesis of Rocksalt-Type MnS from the Polyol Control Reaction Pellet: The pellet from the polyol control reaction, which was suspended in 7.5 mL ethylene glycol, was combined with 598 mg tetramethylammonium hydroxide pentahydrate (3.3 mmol) in a 50 mL 3-neck round bottom flask. This mixture was heated at 120 °C for 10 min. A solution of 67 mg thiourea was dissolve in 7.5 mL ethylene glycol via sonication and injected into the round bottom flask. The reaction mixture was then heated at 160 °C for 2 hours during which the solution developed a seafoam green hue. The reaction mixture was then cooled to room temperature, and the particles were washed with acetone via centrifugation before storing in ethanol.

Characterization

Powder X-ray diffraction (XRD) data were collected using a Bruker D8 Advance X-ray diffractometer using Cu Kα radiation. Transmission electron microscopy (TEM) images were collected from a JEOL 1200 EX II microscope operating at 80 kV.

Results and Discussion

In the standard polyol synthesis, the manganese precursor salt was heated in the presence of tetramethylammonium hydroxide pentahydrate, thiourea, and ethylene glycol. A key step in this synthesis is the decomposition of thiourea which serves as the sulfur source. As has been reported in literature, the decomposition of thiourea to release sulfur requires the presence of both an amine and an alcohol.[16] Both of these requirements are met in the addition of the tetramethylammonium hydroxide pentahydrate (TMAOH). The necessity of the TMAOH was confirmed as its absence prevented nucleation from occurring.

Of the variables studied, reaction temperature, aging time, and the manganese sources proved to have the greatest effect on the resultant crystal phase. Alterations to the solvent as well as the sulfur source resulted in amorphous particles as determined by X-ray diffraction (XRD). This was apparent on the XRD diffractogram through an increased background signal and the absence of defined reflections. When amorphous samples are analyzed via X-ray diffraction, sharp reflections are not seen in the diffractogram because the unordered structure of the material scatters the X-rays at various angles. Additionally, changes to the manganese:sulfur ratio did not impact the crystal phase as rocksalt-type manganese sulfide formed consistently.

Overall, reaction temperature played the largest role in the crystal phase of the products. As is shown in *Figure 6*, the samples formed at lower reaction temperature adopted the rocksalt-type phase whereas the 168 °C sample exhibits wurtzite-type MnS. In addition to the differences in crystal phase, manganese(II) carbonate as well as a manganese layered double hydroxide formed with increasing temperature. The manganese layered double hydroxide is identified by the presence of peaks at $2\theta \approx 11$, 22, and 33°, and the formation of manganese(II) carbonate is believed to result from heating the reaction under a blanket of air. It is also important to note that an amorphous component of the product likely exists due to the high background present in the XRD diffractograms.

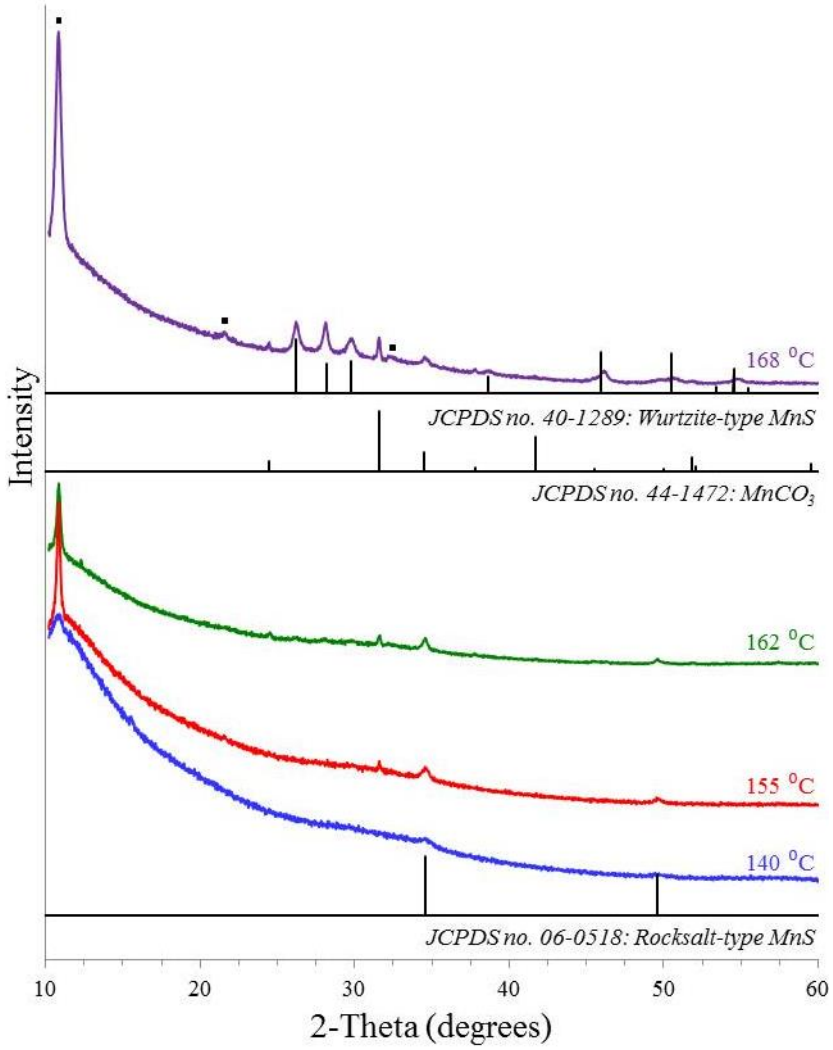

Figure 6: XRD patterns of manganese(II) chloride samples reacted at various temperatures. The squares indicate the presence of a manganese layered double hydroxide.

Similar to reaction temperature, increasing the aging time of a reaction resulted in the formation of both the manganese layered double hydroxide and the manganese(II) carbonate species, *Figure* 7. At the standard reaction time of two hours, a significant peak at 2θ ~11° is observed and remains for the longer 4 hour reaction time. Additional peaks corresponding to manganese(II) carbonate begin to form at 2 hours of aging time and are distinct after 4 hours.

However, in contrast to reaction temperature, rocksalt-type manganese sulfide forms irrespective of aging time.

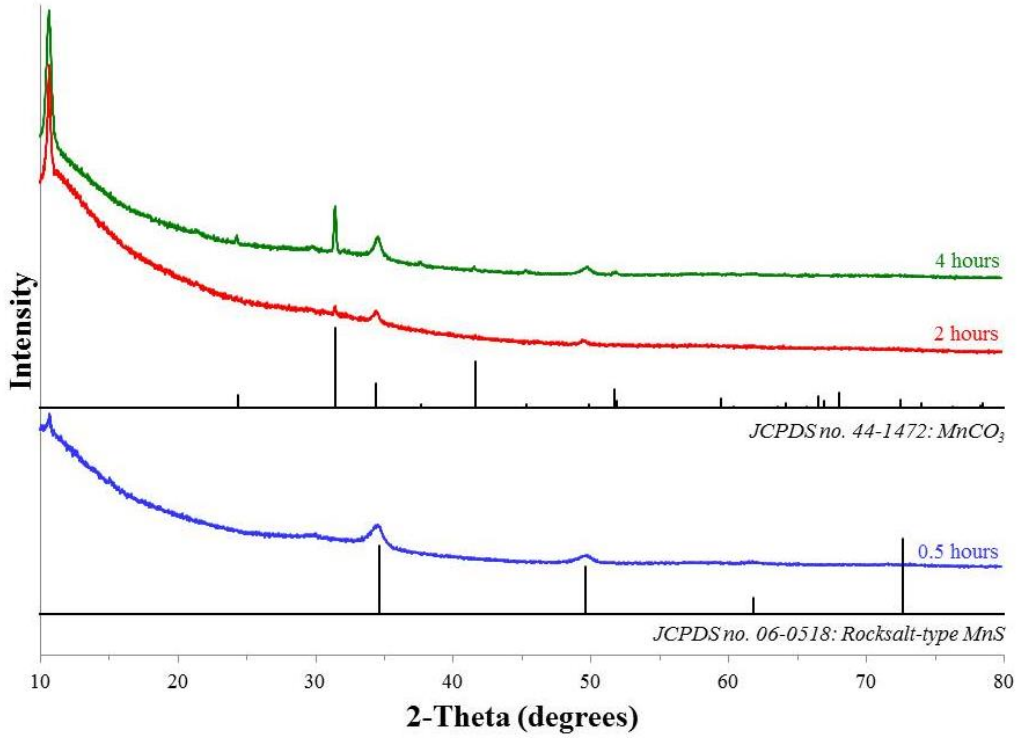

Figure 7: XRD pattern of manganese sulfide samples synthesized with different aging times. The large peak at 2θ ~11° is attributed to a manganese layered double hydroxide.

Interestingly, when the manganese source was changed to manganese(II) acetate, rocksalt-type and wurtzite-type MnS were accessible at lower temperatures with wurtzite-type MnS forming at 140 °C and rocksalt-type MnS forming at 155 °C, *Figure 8*. In addition, a mixed phase sample forms at 168 °C. The use of manganese(II) acetate also seems to impair the formation of the manganese layered double hydroxide as the peak at 2θ ~11° is much less intense for these samples.

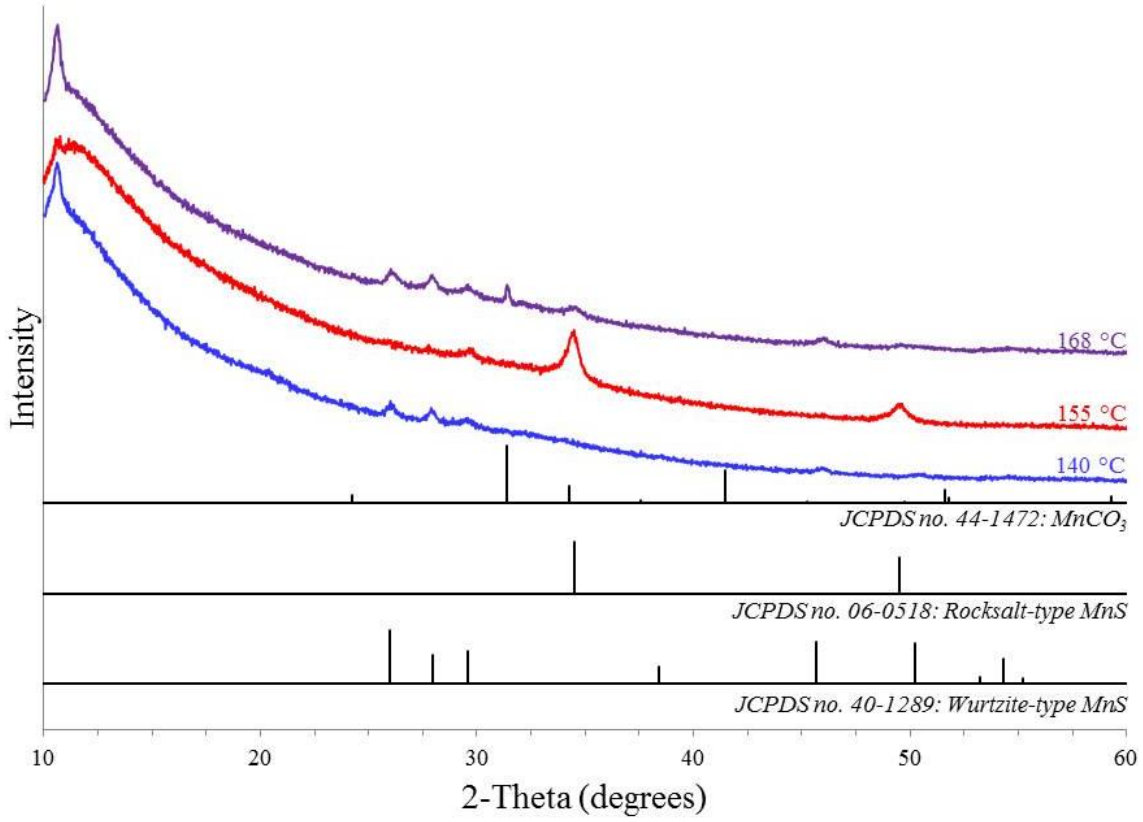

Figure 8: XRD pattern of manganese sulfide particles formed from mangaese(II) acetate at various reaction temperatures.

One disadvantage of the polyol synthesis was the inconsistent morphologies that would result. It was common to see a mix of semi-spherical particles and large sheets (<100 nm in dimensions), *Figure 9*. The sheets were attributed to a manganese layered double hydroxide (LDH) as samples with a more prominent 2θ ~11° peak via XRD had a higher percentage of these sheets when viewed by TEM.

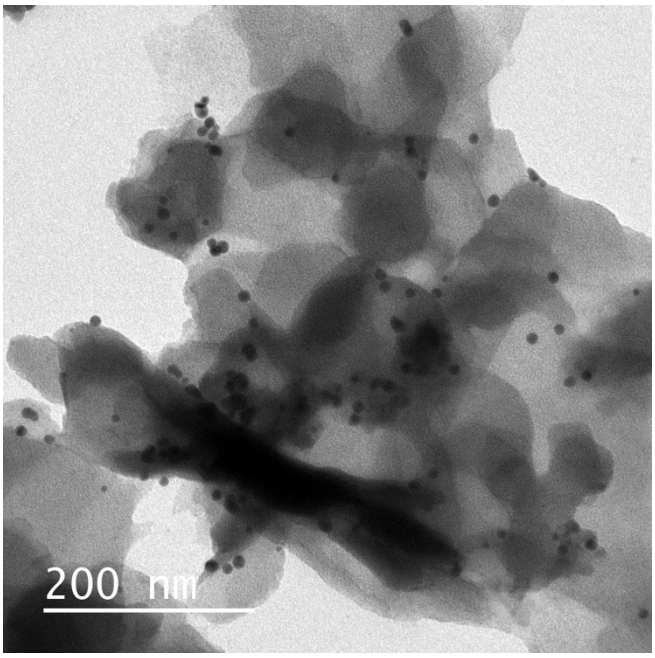

Figure 9: TEM image of a typical MnS sample showing both spherical particles which are attributed to MnS and sheets attributed to a manganese layered double hydroxide.

When reviewing the impact of the different variables, several key facts stand out. In particular, the formation of wurtzite-type MnS at 168 °C whereas rocksalt-type MnS formed at lower temperatures is unexpected. This is because metastable β-MnS and γ-MnS will transform into the thermodynamic α-MnS phase when heated.[4] This suggests that an *in situ* intermediate may be directing the formation of these phases. In contrast to the manganese(II) chloride reactions, when manganese(II) acetate is the manganese source, γ-MnS forms at 140 °C and α-MnS forms at 155 °C. As stated previously, the relative intensities of the reflections at 2θ ~11° also serves as a distinguishing characteristic between the two manganese sources.

Layered double hydroxides (LDH) are materials which have layers of cations interspersed with weakly bound anionic layers for charge balance and adopt the general formula $[M^{2+}_{1-x}M^{3+}_{x}\,(OH)_2]^{x+}(X^{n-})_{x/n} \cdot yH_2O$, *Figure 10*.[17] In the LDH structure, the cations are

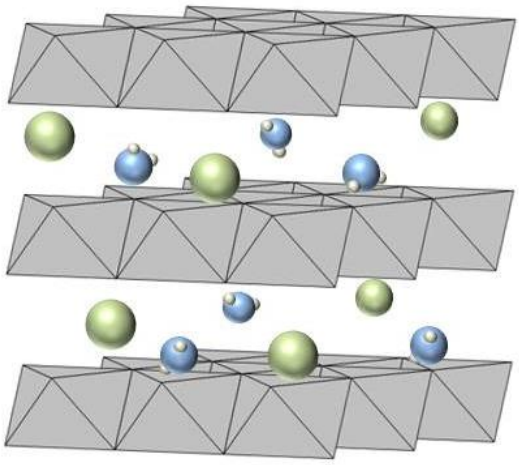

Figure 10: Generic structure of a layered double hydroxide with the grey polyhedral representing the metal hydroxide structure which is then intercalated by green anions for charge balance and blue water molecules. Illustration by Anna E. Powell.

octahedrally coordinated as is also true for the rocksalt crystal structure. Additionally, due to the d-spacing along the c-axis, it is expected that diffraction will occur at low angles which is consistent with the reflection at 2θ ~11° on the XRD patterns. The repetitive reflections every ~11° can be attributed to the stacking of layers within the LDH structure. Furthermore, due to the weakly bound anionic layer of the LDH, exfoliation can easily occur which will lead to formation of sheets with preferred orientation. As a result of preferred orientation, it is expected that only reflections corresponding to the c-axis will be visible via XRD. All of these facts are consistent with both the XRD and TEM data presented for these reactions and led to the belief that these peaks belong to a manganese layered double hydroxide. Finally, a control reaction run in the absence of thiourea led to the exclusive formation of this LDH structure with reflections at ~11, 22, and 33°, *Figure 11*.

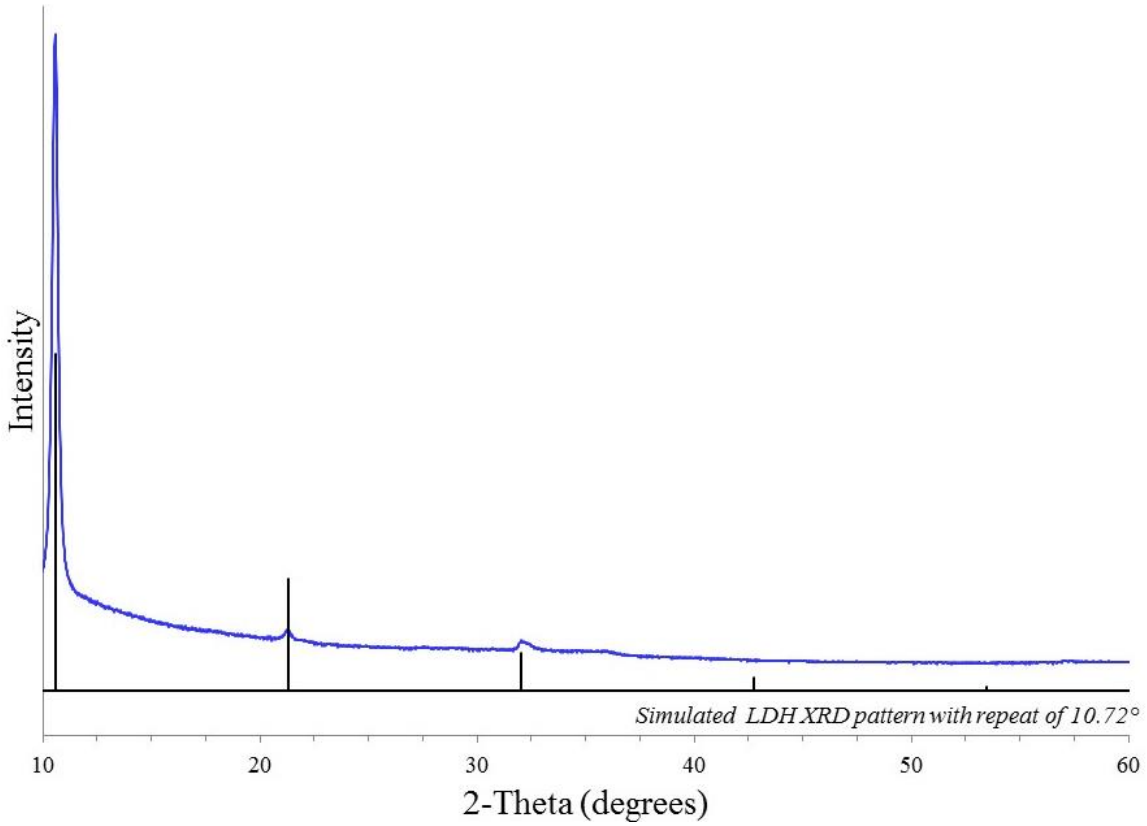

Figure 11: Control reaction run in the absence of thiourea. The resultant pattern is compared to a simulated LDH pattern with a reflection repeat of 10.72°. Additionally, the intensity of the peaks decays at higher degrees 2-Theta.

When considering both the presence of the LDH structure, as well as the unexpected synthesis of α-MnS and γ-MnS, it was hypothesized that formation of the LDH serves as an *in situ* intermediate. As both α-MnS and the manganese LDH share octahedral cation coordination, it was inferred that the LDH templated growth of the thermodynamic phase while the metastable γ-MnS formation was due to the presence of free Mn^{2+} ions in solution. To test this hypothesis, the control experiment was repeated to allow for the formation of the LDH pellet. The pellet from the control reaction was then reacted with thiourea and tetramethylammonium hydroxide pentahydrate (TMAOH) while the supernatant was reacted separately with thiourea and TMAOH. Initial results seemed to support the hypothesis as rocksalt-type MnS did form from

the pellet of the control reaction and wurtzite-type MnS formed from the reaction using the supernatant, *Figure 12*.

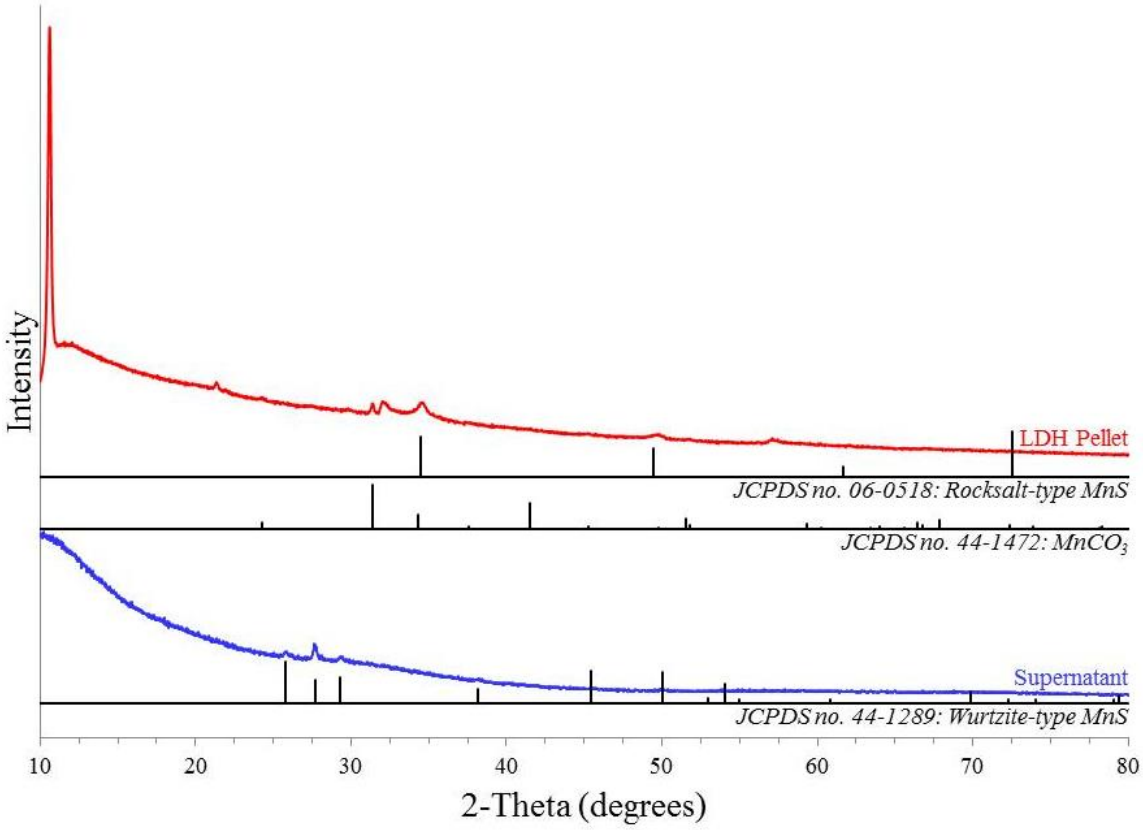

Figure 12: XRD pattern of samples run testing the LDH hypothesis. The top pattern (red) is the sample run containing the manganese LDH pellet. The bottom pattern (blue) is the sample run using the supernatant from the formation of the LDH pellet.

Although initial results seemed to confirm the hypothesis, when the work was repeated with a decreased amount of TMAOH, both α- and γ-MnS formed in the solution containing the pellet. Additionally, with the decreased amount of TMAOH, the reaction run with the supernatant from the control reaction produced rocksalt-type MnS. These results contradict the previously suggested hypothesis. Although the supposed manganese LDH could still be serving as an *in situ* intermediate, it is clear that the concentration of TMAOH and therefore the decomposition rate of thiourea also play key roles in crystal phase determination.

Future Directions

In summary, it was determined that temperature, aging time, and manganese precursor source had the greatest impact on the crystal phase of the product. These results lead to the hypothesis that a manganese layered double hydroxide (LDH) was serving as an *in situ* intermediate to template the growth of rocksalt-type MnS. Although this hypothesis was ultimately disproven, these results did illustrate the influence that the tetramethylammonium hydroxide pentahydrate (TMAOH) and thiourea concentrations, and therefore the sulfur concentration, had on the reaction product.

Preliminary research showed that varying the concentration of thiourea in solution did not influence the reaction product. Therefore, it is likely that a complex relationship between the TMAOH and thiourea concentrations as well as the rate of thiourea decomposition exists. In order to better understand how this relationship may impact crystal phase determination, it is important that the decomposition pathway in terms of this synthesis is studied further.

Another area of future work would be to expand this study to that of solvothermal reactions. To date, phase-pure zinc blende manganese sulfide from colloidal synthesis methods has only been achieved using solvothermal reactions.[18] Additionally, solvothermal synthesis provides the opportunity to decrease unwanted variability as factors like stirring rate are eliminated. Solvothermal synthesis also allows for increased automation to better control variables like heating ramp rate and reaction time which could play subtle roles in crystal phase determination. Finally, the use of solvothermal synthesis allows pressure to be studied as a reaction variable. As is demonstrated by the formation of MnP-type MnS only in high pressure syntheses, pressure is commonly a phase determining factor in nanoscale synthesis.[6] By clarifying the role that such an important variable has in the manganese sulfide reaction, it will

become possible to determine the more subtle roles that other reaction variables may play on crystal phase determination.

References

1. Zhang, X. V.; Martin, S. T.; Friend, C. M. Schoonen, M. A. A.; Holland, H. D. Mineral-Assisted Pathways in Prebiotic Synthesis: Photoelectrochemical Reduction of Carbon(+IV) by Manganese Sulfide. *J. Am. Chem. Soc.* **2004**, *126*, 11247-11253.

2. Kim, D. S.; Lee, J. Y.; Na, C. W.; Yoon, S. W.; Kim, S. Y.; Park, J. Synthesis and Photoluminescence of Cd-doped α-MnS Nanowires. *J. Phys. Chem. B.* **2006**, *110*, 18262-18266.

3. Zhang, N.; Yi, R.; Wang, Z.; Shi, R.; Wang, H.; Qiu, G.; Liu, X. Hydrothermal synthesis and electrochemical properties of alpha-manganese sulfide submicrocrystals as an attractive electrode material for lithium-ion batteries. *Mater. Chem. Phys.* **2008**, *111*, 13-16.

4. Rao, C. N. R.; Pisharody, K. P. R. Transition Metal Sulfides. *Prog. Solid State Chem.* **1976**, *10*, 207-270.

5. Furdyna, J. K.; Samarth, N. Magnetic properties of diluted magnetic semiconductors: A review (invited). *J. Appl. Phys.* **1987**, *61*, 3526-3531.

6. Xiao, G.; Yang, X.; Zhang, X.; Wang, K.; Huang, X.; Ding, Z.; Ma, Y.; Zou, G.; Zou, B. A Protocol to Fabricate Nanostructured New Phase: B31-Type MnS Synthesized under High Pressure. *J. Am. Chem. Soc.* **2015**, *137*, 10297-10303.

7. Michel, F. M.; Schoonen, M. A. A.; Zhang, X. V.; Martin, S. T.; Parise, J. B. Hydrothermal Synthesis of Pure α-Phase Manganese(II) Sulfide without the Use of Organic Reagents. *Chem. Mater.* **2006**, *18*, 1726-1736.

8. Goede, O.; Heimbrodt, W.; Weinhold, V.; Schnürer, E.; Eberle, H. Optical Study of Phase Transition from Tetrahedrally into Octahedrally Coordinated MnS. *Phys. Stat. Sol.* **1987**, *143*, 511-518.

9. Lei, S.; Tang, K.; Yang, Q.; Zheng, H. Solvothermal Synthesis of Metastable γ-MnS Hollow Spheres and Control of Their Phase. *Eur. J. Inorg. Chem.* **2005**, 4124-4128.

10. Joo, J.; Na, H. B.; Yu, T.; Yu, J. H. Kim, Y. W.; Wu, F.; Zhang, J. Z.; Hyeon, T. Generalized and Facile Synthesis of Semiconducting Metal Sulfide Nanocrystals. *J. Am. Chem. Soc.* **2003**, *125*, 11100-11105.

11. Lu, J.; Qi, P.; Peng, Y.; Meng, Z.; Yang, Z.; Yu, W.; Qian, Y. Metastable MnS Crystallites through Solvothermal Synthesis. *Chem. Mater.* **2001**, *13*, 2169-2172.

12. Wang, S. B.; Li, K. W.; Zhai, R.; Wang, H.; Hou, Y. D.; Yan, H. Synthesis of metastable γ-manganese sulfide crystallites by microwave irradiation. *Mater. Chem. Phys.* **2005**, *91*, 298-300.

13. David, L.; Bradford, C.; Tang, X.; Graham, T. C. M.; Prior, K. A.; Cavenett, B. C. Growth of zinc blende MnS and MnS heterostructures by MBE using ZnS as a sulfur source. *J. Cryst. Growth* **2003**, *251*, 591-595.

14. Beltran-Huarac, J.; Resto, O.; Carpena-Nuñez, J.; Jadwisienczak, W. M.; Fonseca, L. F.; Weiner, B. R.; Morell, G. Single-Crystal γ-MnS Nanowires Conformally Coated with Carbon. *ACS Appl. Mater. Interfaces* **2014**, *6*, 1180-1186.

15. Dawood, F.; Schaak, R. E. ZnO-Templated Synthesis of Wurtzite-type ZnS and ZnSe Nanoparticles. *J. Am. Chem. Soc.* **2009**, *131*, 424-425.

16. Rieke, P. C.; Bentjen, S. B. Deposition of Cadmium Sulfide Films by Decomposition of Thiourea in Basic Solutions. *Chem. Mater.* **1993**, *5*, 43-53.

17. Zümreoglu-Karan, B.; Ay, A. N. Layered double hydroxides – multifunctional nanomaterials. *Chem. Pap.* **2012**, *66*, 1-10.

18. Yang, X.; Wang, Y.; Wang, K.; Sui, Y.; Zhang, M.; Li, B.; Ma, Y.; Liu, B.; Zou, Guangtian, Z.; Zou, B. Polymorphism and Formation Mechanism of Nanobipods in Manganese Sulfide Nanocrystals Induced by Temperature or Pressure. *J. Phys. Chem. C.* **2012**, *116*, 3292-3297.

CHAPTER 3. RETENTION OF ANIONIC AND CATIONIC SUBLATTICE FEATURES IN CATION EXCHANGE

Introduction

Often in nanoparticle synthesis, it is desirable to target a specific morphology and/or crystal phase as these are some of the key components that determine material properties. However, this is particularly challenging in polymorphic systems where several different crystal phases can result from only slight alterations to synthetic parameters. Therefore, in order to achieve the goal of targeted synthesis, it is necessary that current synthetic methods are further developed to allow for improved synthetic control.

One method currently used to access a specific metastable phase in polymorphic systems is ion exchange.[1] In this process, the anions or cations of a parent crystal lattice are selectively replaced by a different ionic species while the opposite ion lattice remains intact. As one the lattices remains intact during ion exchange, it can serve as a scaffold helping to template both crystal lattice features and particle morphology. In the case of cation exchange, where the anionic sublattice remains untouched, the crystal phase of the product has traditionally been attributed to the crystal structure of the parent anion sublattice.[2]

However, maintenance of anion sublattice features alone is not enough to provide access to some metastable crystal phases. For example, in the cobalt sulfide system, two crystal phases are accessible – the thermodynamic NiAs-type CoS, and the metastable wurtzite-type CoS, *Figure 13*. Both structures share a hexagonal close packed (hcp) anion sublattice. The two crystal structures differ in that the NiAs crystal structure has octahedral cation coordination whereas the wurtzite crystal structure has tetrahedral cation coordination. Therefore, if a parent nanocrystal with a hcp anion sublattice were used in cation exchange, it is expected that

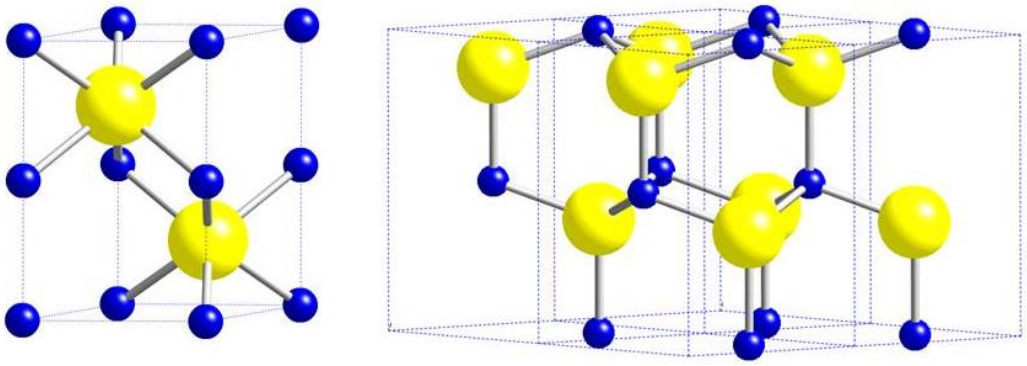

Figure 13: (left) NiAs-type CoS and (right) wurtzite-type CoS. Cobalt ions are blue and sulfur ions are yellow.

thermodynamics would direct the formation of NiAs-type CoS over the metastable wurtzite-type CoS crystal phase. In order to access the metastable wurtzite-type CoS, other factors would have to play a role in the ion exchange.

Another challenge of ion exchange is the limited scope of systems that have been studied. Although cation exchange is frequently cited in systems involving copper, silver, cadmium, lead, and zinc, the majority of transition metals have not been thoroughly explored for ion exchange.[3-5] As a result, the applicability of ion exchange in the majority of transition metal systems is unknown. Beyond limiting the accessibility of potentially interesting metastable phases, this lack of knowledge hinders our ability to better understand ion exchange. Therefore, one goal of this research was to expand cation exchange towards less-studied systems including manganese and cobalt.

Driving Forces of Ion Exchange

There are several driving forces which are generally cited in the feasibility of ion exchange. The first is the short diffusion distances that are inherent in nanomaterials. Although

solid-state diffusion rates can vary greatly depending upon things like crystal structure, defect concentration, and ion size, the diffusion coefficients are generally quite small. Even for systems with comparatively high diffusion coefficients, such as Ag^+ ions in the cubic phase of Ag_2Se, the diffusion coefficient is only ~10^{-5} cm^2/s.[6] Because of this, solid-solid diffusion in bulk samples is generally limited to high-temperature systems which allows for diffusion on an observable time-scale. However, these high-temperature reactions can disrupt the crystal phase and morphology of the material as the more energetic reaction conditions promote rearrangement. In contrast, the small diffusion distances in nanomaterials allow for exchange to occur within a matter of minutes, even at room temperature.

Another driving force frequently cited in ion exchange literature is the tendency of the ions to follow Hard/Soft Acid/Base (HSAB) Theory. HSAB Theory states that hard (Lewis) acids will bind preferentially to hard (Lewis) bases and vice versa. An ion is describe as either "hard" or "soft" based upon the size of its electron cloud. In general, small, highly-charged ions with minimal polarizability are described as "hard" ions, whereas large, highly polarizable species are described as "soft". The preferential binding to species of similar hardness is due to improved orbital overlap between the acid and base.[7] The concepts of HSAB theory can be used to leverage particular ion exchanges through careful selection of coordinating solvents. For example, in order to favor replacement of a relatively soft cation with a harder species, the cationic exchange reaction can be run in a soft solvent such as tri-*n*-octylphosphine (TOP). Conversely, exchange from a harder species to a softer species is favored by completing the exchange in a hard solvent such as methanol.[8] In the following work, TOP was used as the solvent to favor exchange of the relatively soft Cu^+ cations with the harder Co^{2+} and Mn^{2+} ions.

Similarly, methanol was used to favor exchange of the harder Co^{2+} species with the softer Cu^{+} cation.

In the work that follows, we demonstrate the formation of wurtzite-type CoS and MnS nanopartilces via cation exchange from roxbyite-type $Cu_{2-x}S$ precursor. This result is of interest for several reasons. In addition to demonstrating the feasibility of cation exchange with Co^{2+} and Mn^{2+}, the formation of wurtzite-type CoS is noticeable as it was previously only formed through chemical bath deposition.[9] Finally, the formation of these metastable phases led to a hypothesis that both anion and cation sublattice features can be maintained through cation exchange. Although the work presented herein is preliminary and further experimentation is required to validate this hypothesis, these findings have the possibility to transform the way that society thinks of ion exchange.

Experimental

Materials

Manganese(II) chloride tetrahydrate [99% trace metal basis], sulfur powder [-325 mesh, 99.5%], and anhydrous copper(II) chloride [99%] were purchased from Alfa Aesar. Oleylamine [technical grade, 70%], copper(II) acetylacetonate [≥99.9% trace metal basis], di-*tert*-butyl disulfide [97%], and tetrakis(acetonitrile) copper(I) hexafluorophosphate [97%] were purchased from Aldrich. Cobalt(II) chloride [97%] was purchased from Sigma Aldrich. Tri-*n*-octylphosphine [TOP, >85%] was purchased from TCI America. Hexanes, ethanol, methanol, and toluene, all analytical grade, were purchased from VWR. All chemicals were used as received.

Methods

Synthesis of Roxbyite-type $Cu_{2-x}S$ Platelets: Roxbyite-type $Cu_{2-x}S$ platelets were synthesized using a procedure modified from a literature preparation.[10] In a 50 mL 3-neck round bottom flask, 260 mg copper(II) acetylacetonate (0.986 mmol) was combined with 17 mg sulfur powder (0.53 mmol), and 20.0 mL of oleylamine (60.8 mmol). This mixture was degassed for 20 min at room temperature, followed by 20 min at 110 °C using standard Schlenk line techniques. The flask was then placed under an argon blanket and was heated at 200 °C for one hour before cooling to room temperature. The particles were cleaned using hexanes and ethanol and were centrifuged at 12,000 RPM for 3 min. Cleaned particles were then suspended in hexanes, yielding a brown-colored solution.

Synthesis of Copper Sulfide Roxbyite Spheres: Using a method which was adopted from a published preparation,[11] 200 mg copper (II) chloride (1.49 mmol) was combined with 44.2 mL of oleylamine (134 mmol) in a 100 mL 3-neck round bottom flask. The mixture was degassed for 30 minutes each at room temperature and 100 °C using standard Schlenk line techniques. The flask was then placed under an argon flow and was heated at 200 °C for 1 hour. Once the reaction reached ~170 °C, the reaction changed from a dark blue color to a transparent yellow hue. The reaction was then cooled to 180 °C and 6.0 mL of di-*tert*-butyl disulfide (31 mmol) was injected. Shortly after injection, the solution started to darken into a brown-colored solution. The reaction was held at 180 °C for 40 min before cooling to room temperature. The particles were then cleaned with hexanes and ethanol via centrifugation before storing in hexanes. The product solution was a transparent brown color.

Preparation of the Metal-Ion Precursor Solution: Preparation of the metal-ion precursor solution was adapted from a published procedure.[11] A metal-ion precursor solution was formed by combining the metal salt [475 mg cobalt(II) chloride or 725 mg manganese(II) chloride tetrahydrate] with 20 mL oleylamine in a 50 mL 3-neck round bottom flask. The mixture was degassed using standard Schlenk techniques with a slow temperature ramp to 110 °C to control excessive bubbling from degassing. The reaction was then placed under an argon blanket and was heated at 180 °C for 30 min before cooling to approximately 30 °C. At this point, the metal-ion precursor was transferred to a septum-capped vial and purged with argon for storage. Upon cooling to room temperature, the metal-ion precursor solutions solidified and could be stored for several weeks.

Cation Exchange: Cation exchange was performed using an adapted literature preparation.[11] First, the metal-ion precursor solution was heated in a warm water bath under an argon blanket to melt the solid. In a 50 mL 3-neck round bottom flask, 4.0 mL of the metal-ion precursor solution was combined with 15 mL of toluene. This mixture was then placed under an argon blanket and was heated at 100 °C for manganese cation exchange and 110 °C for cobalt cation exchange. Meanwhile, 15 mg of the roxbyite-type $Cu_{2-x}S$ precursor nanocrystals were dried under vacuum and then suspended in 3.5 mL of tri-*n*-octylphosphine (TOP) via sonication. The TOP-roxbyite suspension was then injected into the reaction mixture and the flask was heated for 10 min upon returning to the reaction temperature. The reaction mixture was then cooled to room temperature and cleaned with methanol and toluene via centrifugation before suspending in hexanes. In solution, the manganese exchange product was a light brown color and the cobalt exchange product was black in color.

Re-generation of Roxbyite-type $Cu_{2-x}S$ Platelets from CoS platelets via Ion Exchange: Using a modification of a published procedure,[2] 100 mg of tetrakis(acetonitrile) copper(I) hexafluorophosphate (0.268 mmol) was dissolved in 4.0 mL of methanol via sonication in a scintillation vial to yield a green-colored solution. Meanwhile, the product of the first ion exchange was centrifuged and the excess hexanes were discarded. The resulting pellet was then suspended in 1.0 mL toluene via sonication. The toluene solution was then added to the copper-methanol solution and was sonicated for 10 min to allow for complete exchange. Upon combining the two solutions, the green color of the copper solution changed to brown. The product of the reaction was then cleaned with methanol and toluene via centrifugation before storing in hexanes.

Characterization

Powder X-ray diffraction (XRD) data were collected using a Bruker D8 Advance X-ray diffractometer using Cu Kα radiation. Lattice parameters for wurtzite-type CoS were refined using Jade 2010 manufactured by Materials Data, Inc. Transmission electron microscopy (TEM) images were collected from a JEOL 1200 EX II microscope operating at 80 kV. High-resolution TEM (HRTEM) images, high angle annular dark field scanning TEM (HAADF-STEM) images, and STEM energy dispersive X-ray spectroscopy (STEM-EDS) maps were collected from an FEI Titan^3 G2 S/TEM equipped with spherical aberration correctors on the image and probe-forming lenses at an accelerating voltage of 200 kV. EDS maps were acquired in the FEI Titan^3 using the Super-X EDX quad detector system at a current of ~0.15 nA. Standardless Cliff-Lorimer quantification was performed on the deconvoluted EDS line intensity data using the Bruker Esprit software. ES Vision software (Emispec) was used for EDS data processing.

Results and Discussion

One of the key analytical techniques for this work was X-ray diffraction (XRD) which was used to examine the crystallinity and crystal phase of the synthesized materials. The starting material of the cation exchange reactions was identified as roxbyite-type $Cu_{2-x}S$ and was matched to the pattern PDF 98-000-7965, *Figure 14*.

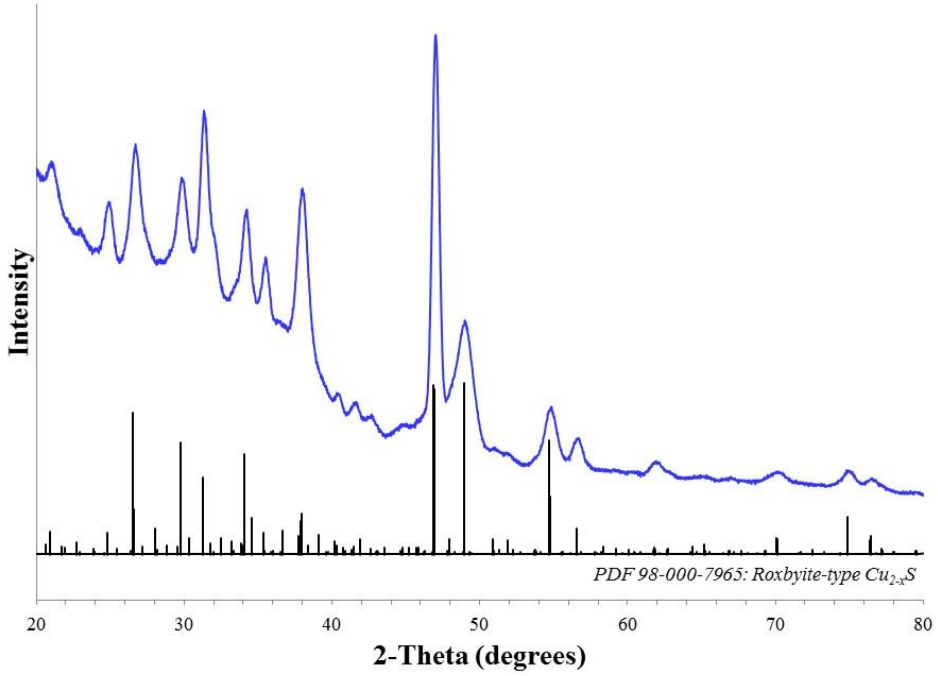

Figure 14: X-ray diffraction pattern of roxbyite-type $Cu_{2-x}S$ platelets.

Roxbyite copper sulfide is a copper-deficient structure with a chemical formula of $Cu_{2-x}S$. The unit cell of roxbyite is monoclinic with lattice parameters of a = 13.4051(9) Å, b = 13.4090(8) Å, and c = 15.4852(3) Å and angles of α = 90.022(2)°, β = 90.021(2)°, and γ = 90.020(3)°.[12] Due to the complexity of the roxbyite crystal structure and resulting XRD pattern, it is impossible to definitively match peaks in the diffractogram to corresponding lattice planes.

The XRD pattern was further analyzed using Scherrer analysis to determine the size of the crystal domain, *Equation 1*.

$$\tau = \frac{K\lambda}{\beta \cos\theta}$$

Equation 1: The Scherrer equation

Originally published in 1918, the Scherrer equation has long been used to determine the mean crystallite size, τ. In the equation, λ is the wavelength of the X-rays used in the diffraction (1.54178 Å for the copper X-ray source used in this analysis), β is the width of the diffraction peak in radians at its half-maximum peak height, and θ is the diffraction angle.[13,14] The most debated term of the Scherrer equation is the shape factor, or K, which is influenced by the shape of the particle. For this analysis, the commonly used approximation of K=0.94 was used.[15] As Scherrer analysis depends upon the width of a diffraction peak, it is important to recognize that many factors, such as instrumental line broadening, contribute to the overall peak width. Therefore, the values determined by Scherrer analysis will likely be slightly smaller than the true particle size.

d-spacing (Å)	2-theta (degrees)	Crystal Domain Size (nm)
3.58	24.9	14.1
3.35	26.7	10.9
3.00	29.8	9.9
2.86	31.3	12.3
2.63	34.2	12.7
2.37	38.0	10.2
1.94	47.0	16.1
1.86	49.0	6.8
1.68	54.8	9.7

Table 1: Scherrer analysis of roxbyite-type $Cu_{2-x}S$ platelets

As is shown in *Table 1*, Scherrer analysis of the prominent roxbyite XRD reflections yielded a crystal domain size ranging from 6.8 nm to 16.1 nm. These values correlate with the

average particle size as determined by TEM. According to TEM, the platelets had an average diameter of 18.6 nm and a thickness of 7.1 nm. The predicted crystal domain sizes fall within these ranges which suggests that the roxbyite platelets are single crystalline. The intermediary domain sizes can be attributed to the crystal planes which do not lie perpendicular to either the side or face of the platelets.

The roxbyite-type platelets were then reacted with a Co^{2+}-oleylamine solution which produced wurtzite-type CoS, *Figure 15.* The experimental XRD pattern is compared to a

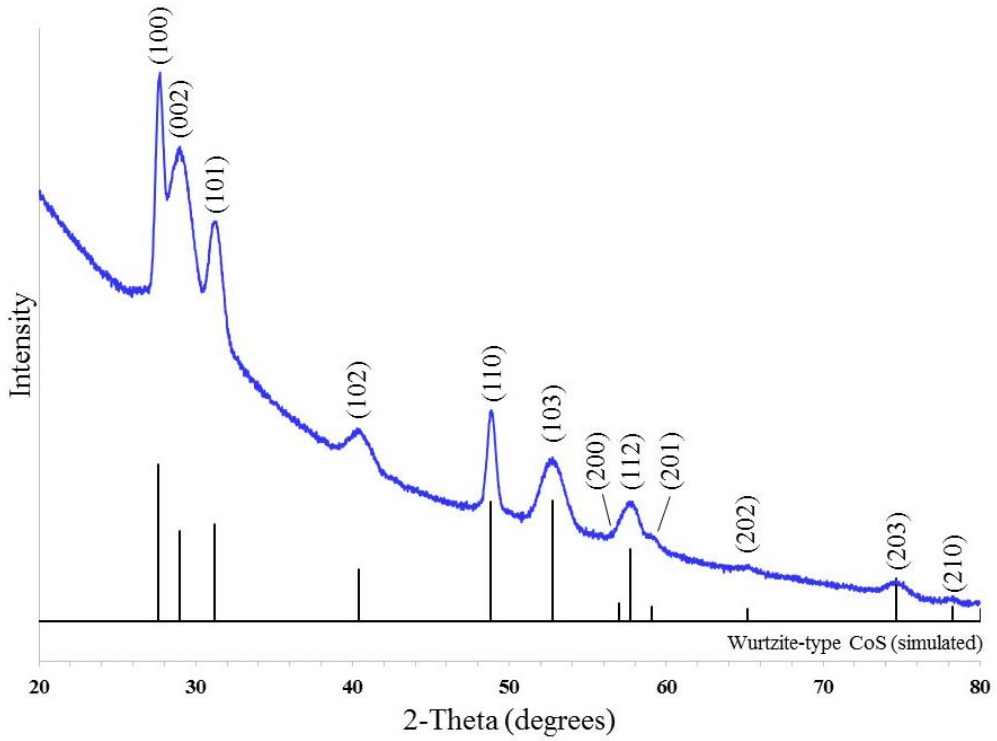

Figure 15: XRD pattern of wurtzite-type CoS platelets compared with a simulated pattern.

simulated pattern for wurtzite-type CoS which was determined using a wurtzite-type ZnS structure pattern (PDF 00-001-0677) as a basis. Rietveld refinement through use of Jade 2010 and whole pattern fitting was then performed to refine the lattice parameters. The resultant refinement indicated a hexagonal unit cell with lattice parameters of a = b = 3.730(2) Å and c =

6.162(2) Å. These lattice parameters are comparable to other wurtzite-type transition metal chalcogenides and follow the expected trends for Shannon-Prewitt ionic radii, *Appendix*. Using these lattice parameters, the wurtzite-type CoS crystal structure was built in CrystalMaker and then an XRD pattern was simulated using CrystalDiffract. The overall particle morphology was retained through the cobalt exchange as is shown through transmission electron microscopy (TEM) images, *Figure 16*. In addition, selected area electron diffraction (SAED) confirms the transition from the roxbyite-type seed particle to the wurtzite-type CoS exchange product.

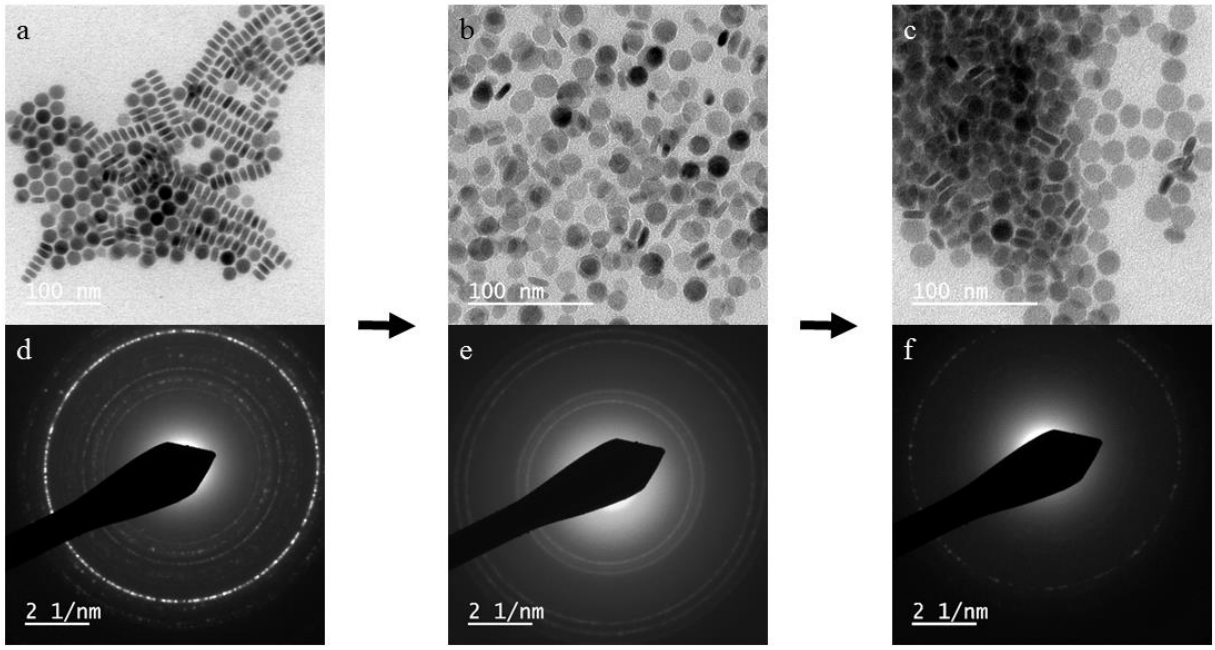

Figure 16: (a) TEM images of the exchange process from the initial roxbyite-type $Cu_{2-x}S$ seed, (b) wurtzite-type CoS, and (c) the reformed roxbyite-type $Cu_{2-x}S$. (d-f) SAED images of the corresponding exchange samples. Image (e) was collected by James M. Hodges.

In addition to cobalt exchange, the wurtzite-type CoS exchange product could be further exchanged with Cu^{+} cations to reform roxbyite-type $Cu_{2-x}S$, *Figure 17*. Although there was a loss of crystallinity in the reformed roxbyite nanocrystals as evidenced by the XRD diffractogram,

the particle morphology was retained across the two exchange processes, *Figure 16*. The reformation of the roxbyite crystal structure is also evidenced through selected-area electron diffraction (SAED).

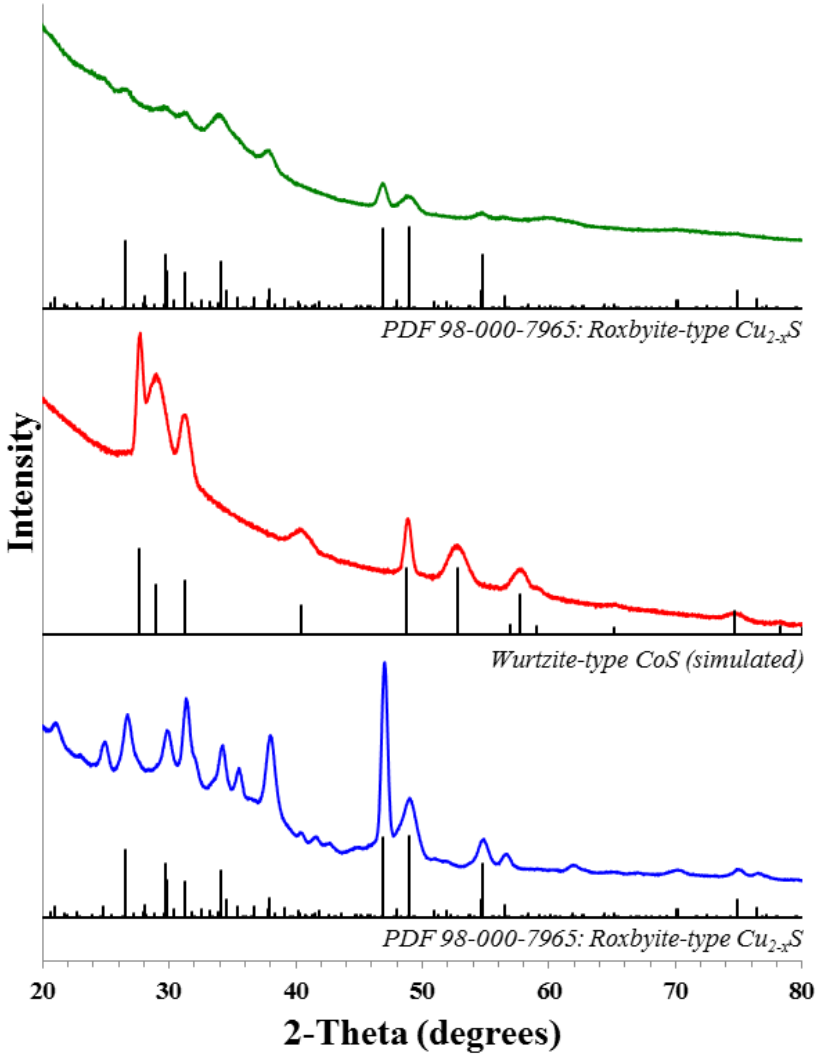

Figure 17: XRD comparison of cation exchange products. Roxbyite-type $Cu_{2-x}S$ seed particles (bottom), wurtzite-type CoS exchange product (middle), and roxbyite-type $Cu_{2-x}S$ reformed upon exchange from CoS (top).

High-resolution transmission electron microscopy (HRTEM) was also used to analyze the Co^{2+} exchange product. Lattice fringes were measured for both the platelet edges and faces. Characteristic images including lattice fringe measurements are shown in *Figure 18.* The

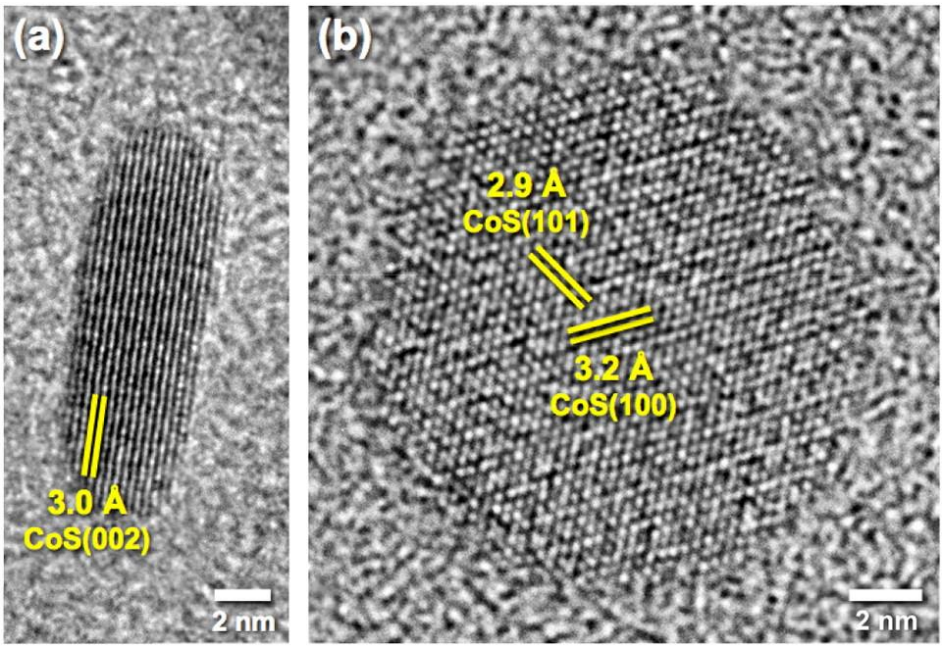

Figure 18: HRTEM image of wurtzite-type CoS showing (a) the edge and (b) the face of the platelets. Images collected by James M. Hodges.

spacing of the platelet edges was measured as 3.0 Å which is consistent with the (002) plane of wurtzite-type CoS. In addition, the face of the platelets shows two planes which intersect at ~ 60°. Lattice spacing for these two planes was measured at 2.9 Å and 3.2 Å which is consistent with the (101) and (100) planes, respectively, of wurtzite-type CoS. Additionally, geometry shows that these planes are expected to intersect at an approximately 60° angle. These lattice assignments are also in agreement with Scherrer analysis, *Table 2*. The (002) plane has a crystallite size of 4.5 nm which is in agreement with the width of the platelets. The (100) plane which is perpendicular to the (002) plane has a crystallite size of 12.7 nm according to Scherrer

Lattice Plane	d-spacing (Å)	2-theta (degrees)	Crystal Domain Size (nm)
(100)	3.24	27.7	12.7
(002)	3.09	29.0	4.5
(101)	2.87	31.2	7.6
(102)	2.23	40.3	5.9
(110)	1.87	48.8	14.9
(103)	1.74	52.8	5.7
(112)	1.60	57.7	7.4

Table 2: Scherrer analysis of wurtzite-type CoS platelets.

analysis which corresponds with the diameter of the platelets. Finally, the (101) plane has an intermediate Scherrer crystallite size of 7.6 nm which is in agreement with the fact that the (101) plane would intersect the face of the platelets at an angle, *Figure 19*.

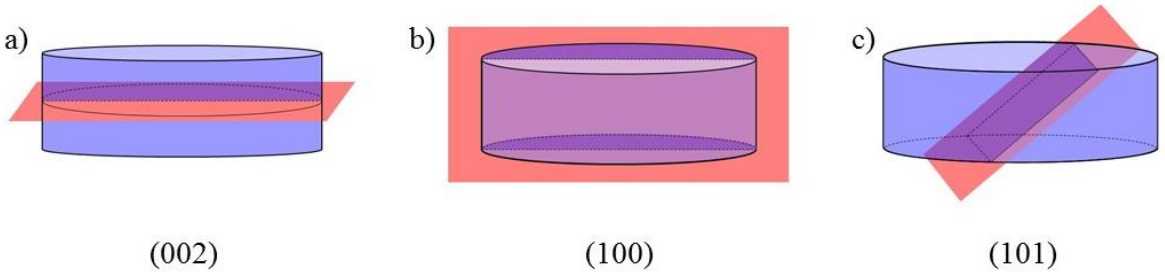

Figure 19: Intersection of lattice planes in the wurtzite-type CoS platelet. (a) the (002) plane dissects the thickness of the platelet and results in a Scherrer crystallite size of 4.5 nm, (b) the (100) plane intersects the nanoplatelet across the face of resulting in a crystallite size of 12.7 nm, and (c) the (101) plane intersects the face the platelet at an angle resulting in an intermediate crystallite size of 7.6 nm.

Finally, the wurtzite-type CoS platelets were analyzed using energy-dispersive X-ray spectroscopy (EDS). STEM-EDS elemental mapping of the CoS platelets for three elements of interest is shown in *Figure 20* along with a high-angle annular dark field (HAADF) STEM image. The STEM-EDS elemental mapping indicates that the exchange was complete with only residual copper present on the grid.

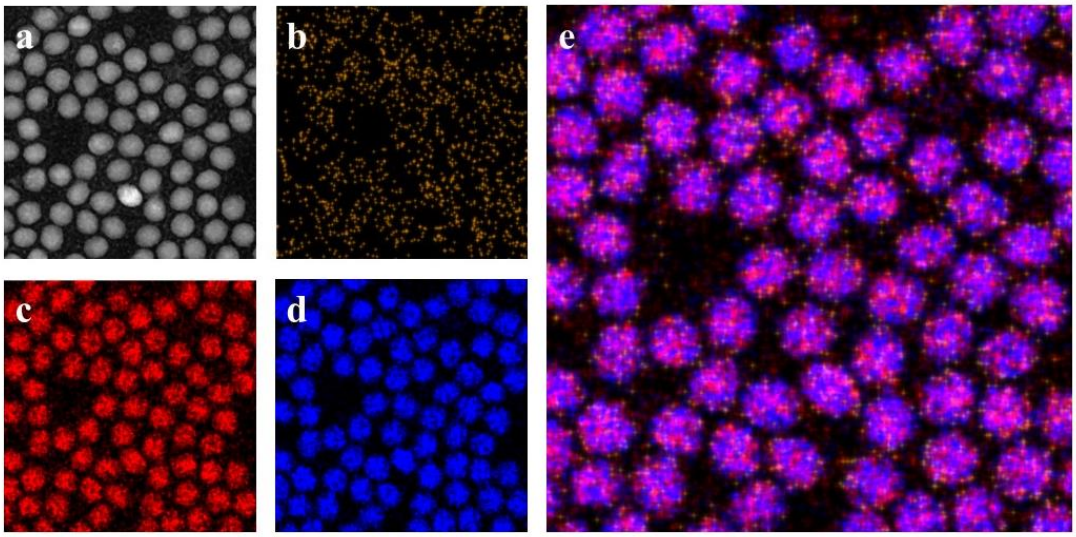

Figure 20: (a) HAADF-STEM image of wurtzite-type CoS platelets. STEM-EDS elemental maps of the CoS platelets for: (b) copper, (c) cobalt, (d) sulfur, and (e) overlay of copper, cobalt, and sulfur. Images collected by James M. Hodges.

An EDS spectrum of the wurtzite-type CoS platelets was also collected and is shown in *Figure 21*. As expected, there is a large signal from cobalt and sulfur. There is also a large

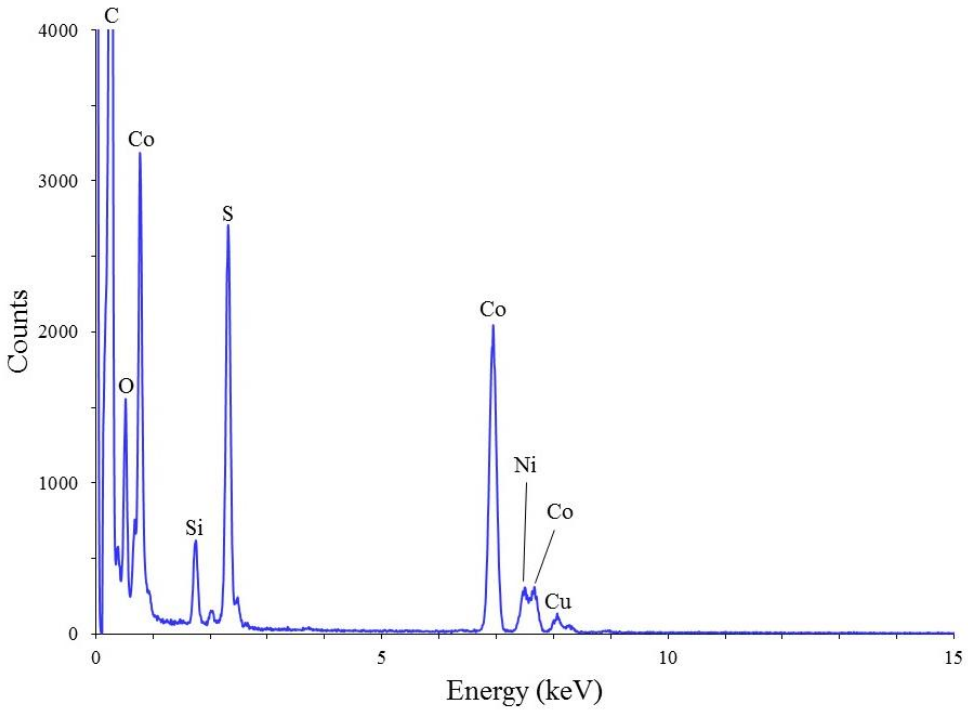

Figure 21: EDS spectrum of wurtzite-type CoS platelets. Data collected by James M. Hodges.

signal from native carbon as well as smaller signals from silicon, oxygen, and nickel which can be attributed to the silicon sample holder, the intrinsic presence of oxygen, and the use of a nickel grid. A small signal from residual copper is also present, ~1%. This signal could be due to residual copper ions in the particles and/or copper ions which exchange out of the crystal lattice but remained in the solution after exchange. As the product suspension was later drop-cast onto the grids, this residual copper would then have been introduced to the grids.

Although the formation of wurtzite-type CoS has been confirmed using several techniques, it is nonetheless surprising that metastable wurtzite-type CoS forms rather than the thermodynamically stable NiAs-type CoS.[16] In cation exchange, the anion sublattice is frequently cited as a phase determining factor. In roxbyite, the sulfur atoms adopt a distorted hexagonal-close packed (hcp) anion sublattice, *Figure 22*. Therefore, it is expected that the

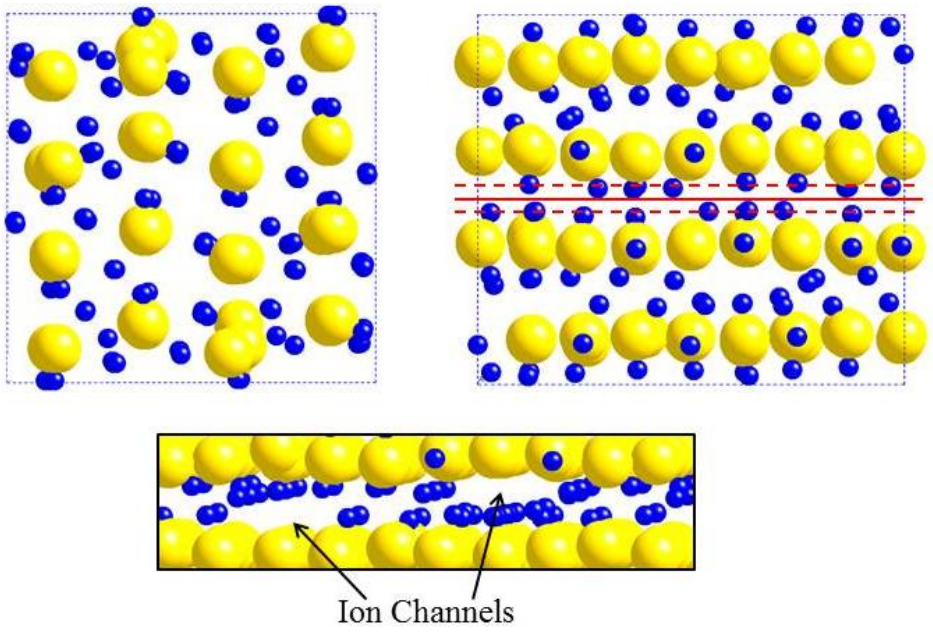

Figure 22: Roxbyite-type $Cu_{2-x}S$ where blue denotes copper cations and yellow denotes sulfur anions. (Top Left) View of roxbyite-type $Cu_{2-x}S$ along the (001) plane depicting a distorted hcp anion sublattice. (Top Right) View of roxbyite-type $Cu_{2-x}S$ along the (010) plane. The solid red line dissecting the (010) plane indicates the octahedral holes, and the two dotted red lines indicate tetrahedral holes. (Bottom) Magnification of the ion channels present along the (010) plane.

product of the cation exchange would also exhibit an hcp anion sublattice. Although wurtzite has an hcp anion sublattice, so does the nickel arsenide crystal structure. Therefore, the hcp anion sublattice of roxbyite is not the sole phase determining factor in this exchange. When comparing the wurtzite crystal structure to that of nickel arsenide, the distinguishing characteristic is the cation coordination. In nickel arsenide, the cations are octahedrally coordinated; in wurtzite, the cations are tetrahedrally coordinated, *Figure 13*.

Upon further study of the roxbyite crystal structure, *Figure 22*, it becomes clear that the copper ions predominantly occupy tetrahedral holes while the octahedral holes remain open. This led to the hypothesis that both anion and cation sublattice features in the form of the hcp anion sublattice and the cation occupation of the tetrahedral holes direct the formation of the wurtzite exchange product. It is also believed that the vacancies in the roxbyite crystal structure, denoted by the black arrows in *Figure 22* may serve as ion channels aiding in cation diffusion during exchange.

The hypothesis that both anion and cation sublattice features can be maintained during cation exchange was tested through ion exchange of roxbyite-type $Cu_{2-x}S$ with other 3d transition metal cations, namely manganese. Manganese sulfide is an ideal model system for this reaction as it forms three distinct crystal phases: the thermodynamic rocksalt phase as well as the two metastable phases, wurtzite and zinc blende. Rocksalt has a cubic-close packed anion sublattice with octahedrally coordinated cations. Zinc blende also has a cubic-close packed anion sublattice but the cations are tetrahedrally coordinated.

In order to test the hypothesis of dual cation and anion sublattice feature retention, roxbyite-type $Cu_{2-x}S$ seed particles were reacted with Mn^{2+}-oleylamine to produce wurtzite-type MnS. As hypothesized, both anion and cation sublattice features of the roxbyite were retained

and wurtzite-type MnS formed as confirmed via XRD, *Figure 23.* The XRD pattern shown in *Figure 23* is from a sample that did not maintain particle morphology. However, it distinctly shows the wurtzite-type MnS pattern. Other samples maintained the platelet morphology; however, their associated XRD patterns were not as distinct.

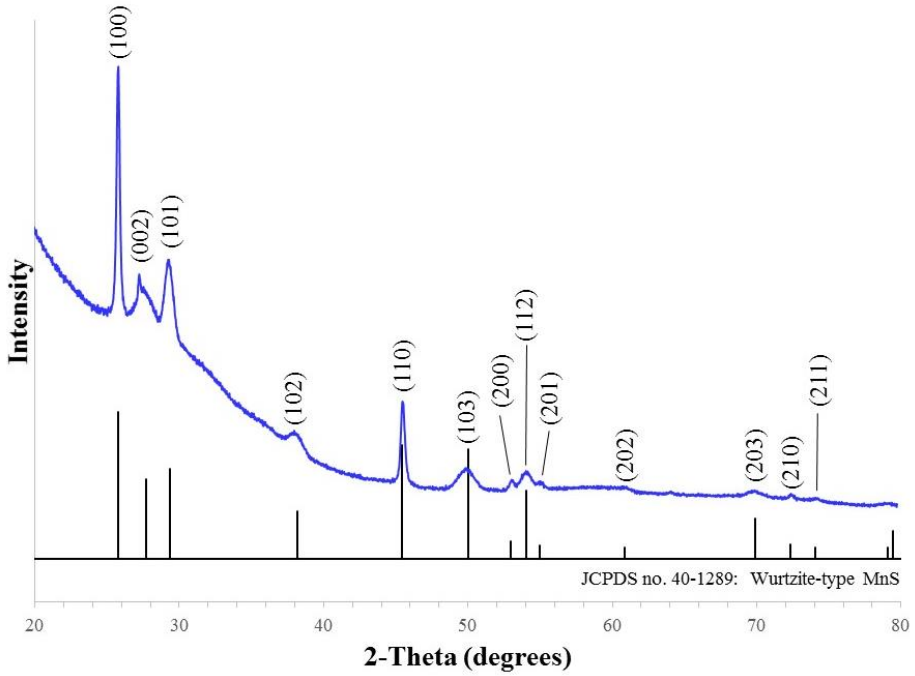

Figure 23: XRD pattern of wurtzite-type MnS platelets which were formed via cation exchange from roxbyite-type $Cu_{2-x}S$.

For comparison, a representative wurtzite-type MnS sample that maintained the platelet morphology was analyzed via TEM and SAED, and the resultant images are shown in *Figure 24*. This sample was also analyzed by STEM-energy-dispersive X-ray spectroscopy (STEM-EDS), *Figure 25*. As expected, the spectra had signals from manganese and sulfur as well as smaller signals from carbon, oxygen, and silicon. In contrast with the cobalt exchange product which contained only ~1% copper, the MnS product contained ~12% copper. Although the possible

role of this residual copper is unknown at this time, the remaining copper could play a role in the stability of the product.

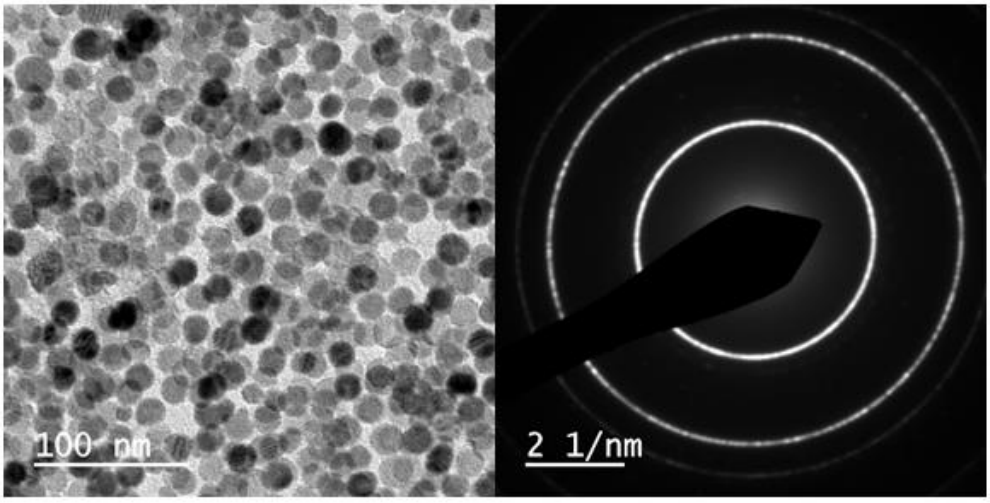

Figure 24: (left) TEM image and (right) SAED of wurtzite-type MnS platelets.

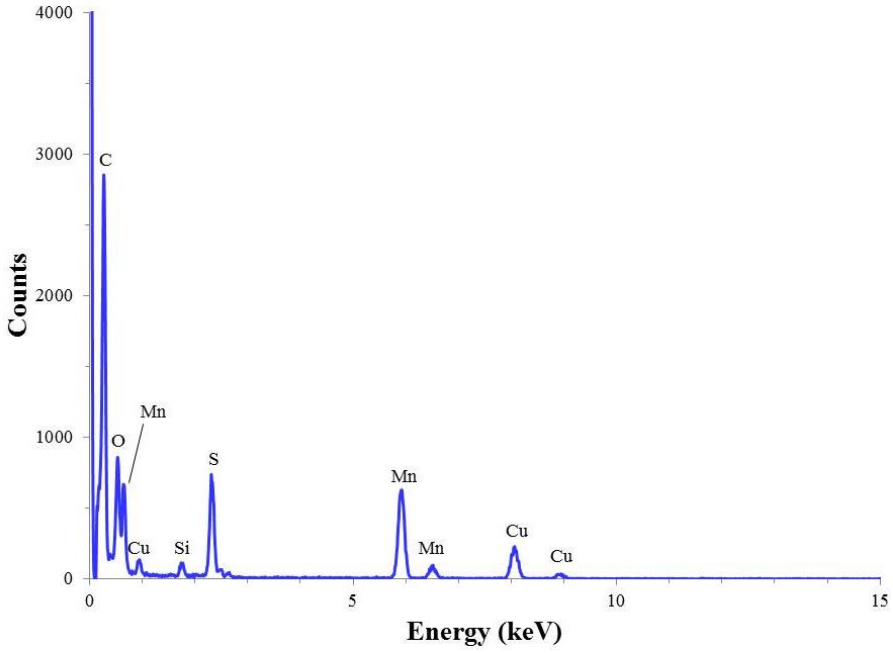

Figure 25: EDS spectra of wurtzite-type MnS platelets. Unlike the CoS sample, a significant amount of copper, ~12%, remains after the exchange. Data collected by James M. Hodges.

In addition to the roxbyite-type $Cu_{2-x}S$ platelets, roxbyite-type spheres were also synthesized and analyzed via XRD and TEM, *Figure 26.* It should be noted that more reflections

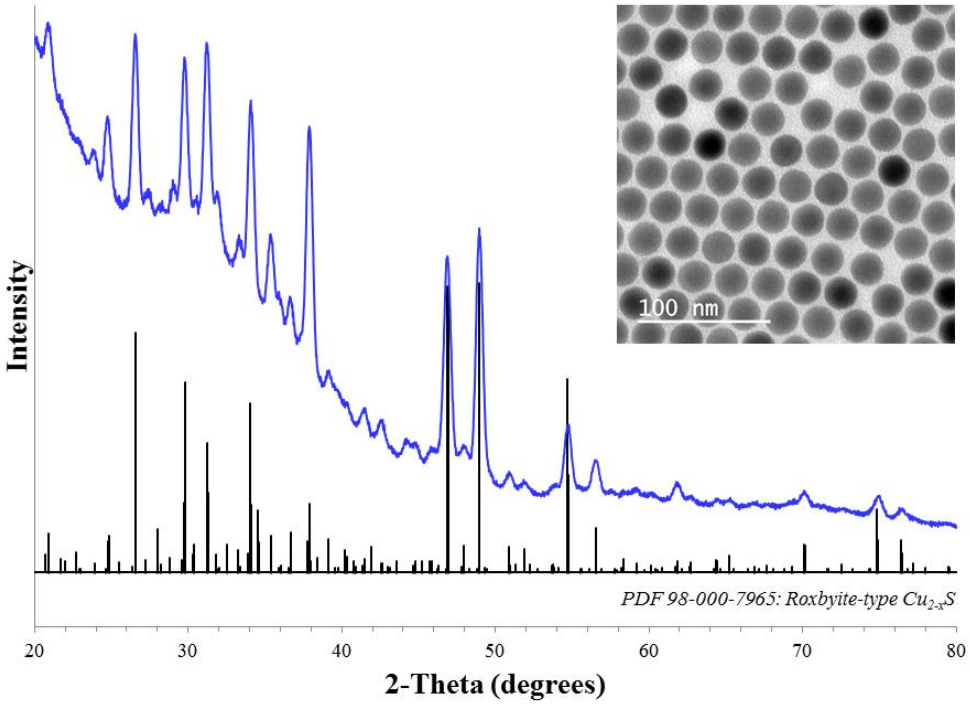

Figure 26: XRD of roxbyite-type $Cu_{2-x}S$ spheres. Inset is a TEM image of the roxbyite-type spheres.

are present in the X-ray diffractogram of the roxbyite-type spheres than the platelets, *Figure 14*. This is likely due to preferred orientation in the platelet sample which causes stronger intensities of certain reflections and weaker intensities of other reflections depending upon the orientation of the sample on the XRD plate.

The roxbyite-type $Cu_{2-x}S$ spheres were also used as seed particles in cation exchange to produce wurtzite-type CoS spheres with morphological retention as shown in *Figure 27*. Although the exchange did occur with the roxbyite spheres, there was a significant loss of crystallinity during the cobalt exchange. It is hypothesized that this loss of crystallinity is due to

the morphology of the particles. Compared to the spheres, the platelets allow for a shorter diffusion distance which could result in increased crystallinity. In addition, it is possible that face of the platelets is a more favorable surface for the exchange process and the larger area facilitates the exchange.

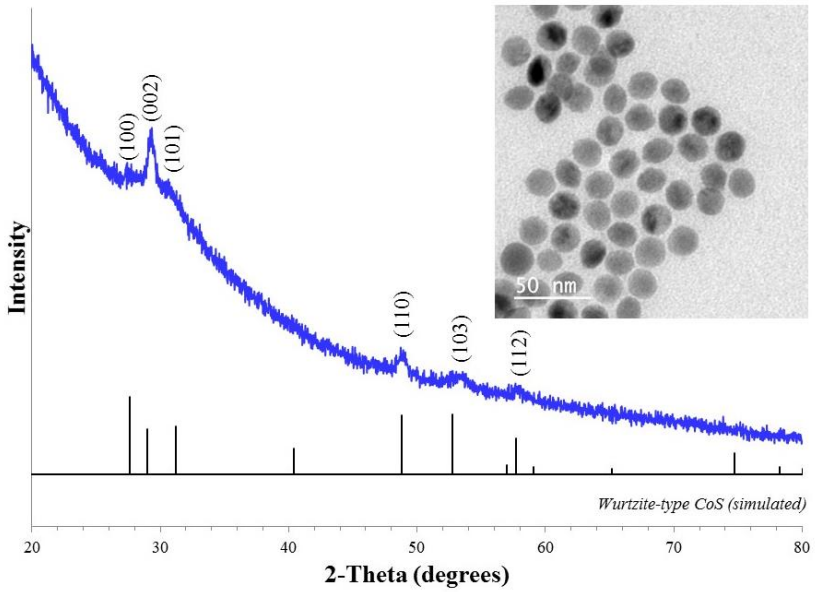

Figure 27: XRD pattern of wurtzite-type CoS. Inset is a TEM image of the exchange product.

In order to confirm that the cobalt exchange was complete, the wurtzite-type CoS spheres were analyzed via EDS-STEM elemental mapping and HAADF-STEM and the images are shown in *Figure 28.*

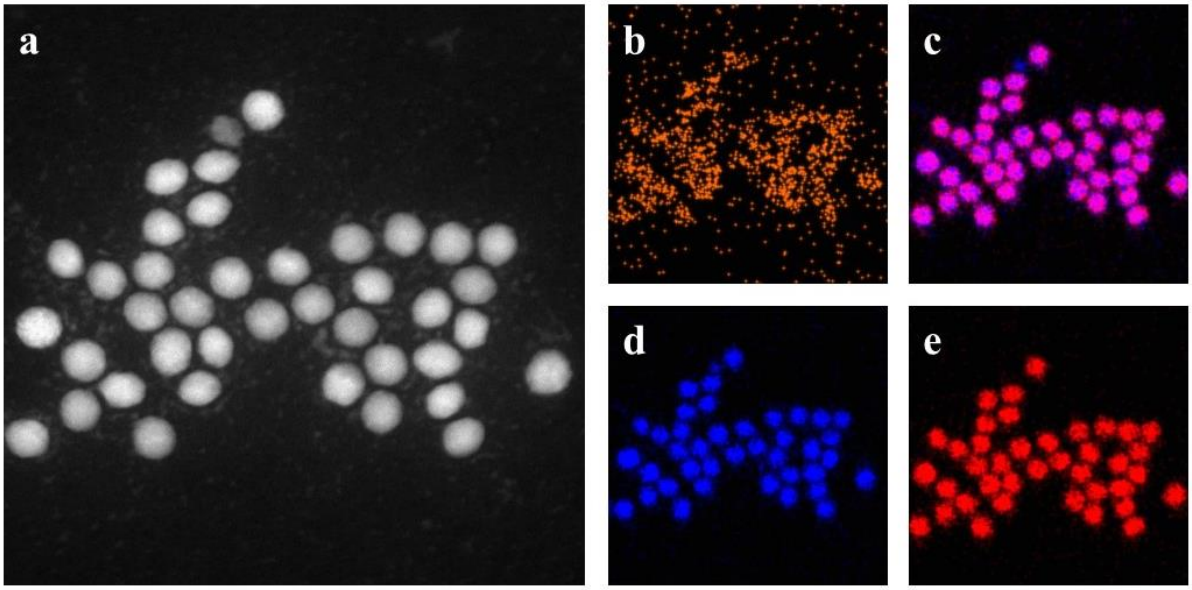

Figure 28: (a) High-angle annular dark field (HAADF) STEM of wurtzite-type CoS spheres. Energy-dispersive X-ray spectroscopy (EDS) STEM elemental mapping of wurtzite-type CoS spheres: (b) copper, (c) cobalt and sulfur overlay, (d) cobalt, and (e) sulfur. Data collected by James M. Hodges.

Future Directions

In summary, wurtzite-type CoS, rather than the thermodynamically stable NiAs-type CoS crystal phase, was formed via ion exchange from roxbyite-type $Cu_{2-x}S$. As a result, it is hypothesized that both anionic and cationic sublattice features can be maintained in cation exchange. This hypothesis is further supported through the formation of wurtzite-type MnS upon cation exchange and can also be expanded to encompass seed particles of different morphologies.

The results herein pose significant advances in understanding the process of ion exchange. By furthering knowledge in this area, it becomes possible to gain greater synthetic control of colloidal nanoparticle systems. Therefore, it is imperative that future work tries to

build upon the results shown herein and attempt to further elucidate the underlying mechanisms at play in ion exchange.

First of all, it is recommended that cobalt exchange of roxbyite-type $Cu_{2-x}S$ be repeated allowing for only partial cation exchange. For this initial research, full cation exchange was targeted in order to prove the feasibility of cation exchange with previously understudied 3d transition metals and later to elucidate the possible retention of both cation and anion sublattice features. Investigations using partial cation exchange would be beneficial as this would provide a preliminary indication of the most reactive crystallographic faces as it would indicate which segments of the seed particle undergo exchange first.[16] These results could lead towards insight into the improved crystallinity of the platelet samples over the spheres as morphology may be a key consideration for cation exchange.

It is also possible that the insight gained from partial cation exchange of the roxbyite seed particles could lead towards a more physical understanding of cation exchange in this system. When observing the roxbyite crystal structure, it was suggested that the presence of channels could aid in cation diffusion within the structure. Although it is difficult to identify the exact orientation of planes in roxbyite due to the complexity of its crystal structure, it is possible that the results of the partial exchange could be correlated with the roxbyite structure to see if these proposed channels run in a direction that would aid cation diffusion. If so, other crystal structures with similar channels could be investigated for cation exchange to see what role channels might play in ion diffusion and exchange.

Finally, although this research is significant for several reasons, it is important to specifically recognize the role that this work plays in expanding the scope of cation exchange. As was previously mentioned, full cation exchange has traditionally been limited to a number of

highly studied systems including: copper, silver, cadmium, and zinc. This work expands the known exchange capabilities of cobalt and manganese from mere dopants to species that can be used in full cation exchange.[17,18] As a result, it is now possible to access a broader range of materials via cation exchange. In order to build upon this success and further expand the applicability of ion exchange, it is important that more studies continue to explore ion exchange with non-traditional species.

References

1. Li, H.; Zanella, M.; Genovese, A.; Povia, M.; Falqui, A.; Giannini, C.; Manna, L. Sequential Cation Exchange in Nanocrystals: Preservation of Crystal Phase and Formation of Metastable Phases. *Nano. Lett.* **2011**, *11*, 4964-4970.

2. Prashant K. Jain, L. A., Shaul Aloni and A. Paul Alivisatos, Nanoheterostructure Cation Exchange: Anionic Framework Conservation. *J. Am. Chem. Soc.* **2010,** *132* (29), 9997-9999.

3. Luther, J. M.; Zheng, H.; Sadtler, B.; Alivisatos, A. P. Synthesis of PbS Nanorods and Other Ionic Nanocrystals of Complex Morphology by Sequential Cation Exchange. *J. Am. Chem. Soc.* **2009**, *131*, 16851-16857.

4. Miszta, K.; Dorfs, D.; Genovese, A.; Kim, M. R.; Manna, L. Cation Exchange Reactions in Colloidal Branched Nanocrystals. *ACS Nano.* **2011**, *5*, 7176-7183.

5. Camargo, P. H. C.; Lee, Y. H.; Jeong, U.; Zou, Z.; Xia, Y. Cation Exchange: A simple and Versatile Route to Inorganic Colloidal Spheres with the Same Size but Different Compositions and Properties. *Langmuir* **2007**, *23*, 2985-2992.

6. Son, D. H.; Hughes, S. M.; Yin, Y.; Alivisatos, A.P. Cation Exchange Reactions in Ionic Nanocrystals. *Science*. **2004**, *306*, 1009-1012.

7. Pearson, R. G. Hard and Soft Acids and Bases. *J. Am. Chem. Soc.* **1963**, *85* (22), 3533-3539.

8. Beberwyck, B. J.; Surendranath, Y.; Alivisatos, A. P. Cation Exchange: A Versatile Tool for Nanomaterial Synthesis. *J. Phys. Chem. C.* **2013**, *117*, 19759-19770.

9. Mane, S. T.; Kamble, S. S.; Deshmukh, L. P. Cobalt sulphide thin films: Chemical bath deposition, growth and properties. *Mater. Lett.* **2011**, *65*, 2639-2641.

10. Mona Lotfipour, T. M., Daniel P. Rossi, and Katherine E. Plass, α-Chalcocite Nanoparticle Synthesis and Stability. *Chem. Mater.* **2011,** *23* (12), 3032-3038.

11. Don-Hyung Ha, A. H. C., Matthew J. Ward, Shreyas Honrao, Kiran Mathew, Robert Hovden, Margaret K. A. Koker, David A. Muller, Richard G. Hennig, and Richard D. Robinson, Solid–Solid Phase Transformations Induced through Cation Exchange and Strain in 2D Heterostructured Copper Sulfide Nanocrystals. *Nano. Lett.* **2014,** *14* (12), 7090-7099.

12. Mumme, W. G.; Gable, R. W.; Petříček, V. The Crystal Structure of Roxbyite, $Cu_{58}S_{32}$. *Can. Mineral.* **2012**, *50*, 423-430.

13. Scherrer, P. Bestimmung der Grösse und der inneren Struktur von Kolloidteilchen mittels Röntgenstrahlen. *Göttinger Nachrichten Math. Phys.* **1918**, *2*, 98–100.

14. Holzwarth, U.; Gibson, N. The Scherrer equation versus the 'Debye-Scherrer equation.' *Nat. Nanotechnol.* **2011**, *6*, 534.

15. Langford, J. I.; Wilson, A. J. C. Scherrer after Sixty Years: A Survey and Some New Results in the Determination of Crystallite Size. *J. Appl. Cryst.* **1978**, *11*, 102-113.

16. Villars, P. *Pearson's Handbook: Desk Edition*, 1st Ed.; ASM International: Materials Park, OH, 1997.

17. Sadtler, B.; Demchenko, D. O.; Zheng, H.; Hughes, S. M.; Merkle, M. G.; Dahmen, U.; Wang, L.-W.; Alivisatos, A. P. Selective Facet Reactivity during Cation Exchange in Cadmium Sulfide Nanorods. *J. Am. Chem. Soc.* **2009**, *131*, 5285-5293.

18. Sytnyk, M.; Kirchschlager, R.; Bodnarchuk, M. I.; Primetzhofer, D.; Kriegner, D.; Enser, H.; Stangl, J.; Bauer, P.; Voith, M.; Hassel, A. W.; Krumeich, F.; Ludwig, F.; Meingast, A.; Kothleitner, G.; Kovalenko, M. V.; Heiss, W. Tuning the Magnetic Properties of Metal Oxide Nanocrystal Heterostructures by Cation Exchange. *Nano. Lett.* **2013**, *13*, 586-593.

19. Eilers, J.; Groeneveld, E.; Donegá, C. M.; Meijerink, A. Optical Properties of Mn-Doped ZnTe Magic Size Nanocrystals. *J. Phys. Chem. Lett.* **2012**, *3*, 1663-1667.

Appendix: Comparison of Wurtzite-Type Transition Metal Chalcogenides

	MnO[1]	**CoO**[2]	**ZnO**[2]	**MnS**[2]	**CoS**[3]	**ZnS**[2]
a = *b* =	3.3718(2)	3.21	3.2475	3.9792	3.730(2)	3.8227
c =	5.3854(7)	5.24	5.2042	6.4469	6.162(2)	6.2607

Table 3: Lattice parameters (Å) for various wurtzite-type transition metal chalcogenides.

Ion Species	**Crystal Radii (pm)**
Co^{2+}	72
Cu^{+}	74
Mn^{2+}	80
Zn^{2+}	74

Table 4: Shannon-Prewitt ionic radii of tetrahedrally coordinated cations.[4]

References

1. Nam, K. M.; Kim, Y.-I.; Jo, Y.; Lee, S. M.; Kim, B. G.; Choi, R.; Choi, S.-I.; Song, H.; Park, J. T. New Crystal Structure: Synthesis and Characterization of Hexagonal Wurtzite MnO. *J. Am. Chem. Soc.* **2012**, *134*, 8392-8395.

2. Villars, P. *Pearson's Handbook: Desk Edition*, 1st Ed.; ASM International: Materials Park, OH, 1997.

3. Experimentally determined values

4. Shannon, R. D. Revised Effective Ionic Radii and Systematic Studies of Interatomic Distances in Halides and Chalcogenides. *Acta. Cryst.* **1976**, *A32*, 751-767.